

## Article

# Ore Genesis of the Baishitouwa Quartz–Wolframite Vein-Type Deposit in the Southern Great Xing’an Range W Belt, NE China: Constraints from Wolframite In-Situ Geochronology and Geochemistry Analyses

Wei Xie <sup>1,2,3</sup> , Qingdong Zeng <sup>1,2,3,\*</sup>, Lingli Zhou <sup>4</sup>, Tingguang Lan <sup>5</sup>, Ruiliang Wang <sup>6</sup> and Jinjian Wu <sup>1,2,3</sup>

- <sup>1</sup> Key Laboratory of Mineral Resources, Institute of Geology and Geophysics, Chinese Academy of Sciences, Beijing 100029, China; xiewei20@mails.ucas.ac.cn (W.X.); wujinjian19@mails.ucas.ac.cn (J.W.)
- <sup>2</sup> Innovation Academy for Earth Science, Chinese Academy of Sciences, Beijing 100029, China
- <sup>3</sup> College of Earth and Planetary Sciences, University of Chinese Academy of Sciences, Beijing 100049, China
- <sup>4</sup> Earth and Ocean Sciences and Irish Centre for Research in Applied Geosciences (iCRAG), National University of Ireland, H91TK33 Galway, Ireland; lingli.zhou@icrag-centre.org
- <sup>5</sup> State Key Laboratory of Ore Deposit Geochemistry, Institute of Geochemistry, Chinese Academy of Sciences, Guiyang 550081, China; lantingguang@126.com
- <sup>6</sup> Faculty of Geosciences and Resources, China University of Geosciences (Beijing), Beijing 100083, China; rlwang@cugb.edu.cn
- \* Correspondence: zengqingdong@mail.iggcas.ac.cn



**Citation:** Xie, W.; Zeng, Q.; Zhou, L.; Lan, T.; Wang, R.; Wu, J. Ore Genesis of the Baishitouwa Quartz–Wolframite Vein-Type Deposit in the Southern Great Xing’an Range W Belt, NE China: Constraints from Wolframite In-Situ Geochronology and Geochemistry Analyses. *Minerals* **2022**, *12*, 515. <https://doi.org/10.3390/min12050515>

Academic Editors:  
Yamirka Rojas-Agramonte and  
António Manuel Nunes Mateus

Received: 30 March 2022

Accepted: 15 April 2022

Published: 21 April 2022

**Publisher’s Note:** MDPI stays neutral with regard to jurisdictional claims in published maps and institutional affiliations.



**Copyright:** © 2022 by the authors. Licensee MDPI, Basel, Switzerland. This article is an open access article distributed under the terms and conditions of the Creative Commons Attribution (CC BY) license (<https://creativecommons.org/licenses/by/4.0/>).

**Abstract:** The Baishitouwa deposit is a medium-scale quartz–wolframite vein-type deposit in the southern Great Xing’an Range tungsten (W) belt. The W mineralization occurs mainly as veins and dissemination within the mica schist of the Mesoproterozoic Baiyunebo Group. The formation of the deposit can be divided into four stages. The wolframite yielded a lower intercept  $^{206}\text{Pb}/^{238}\text{U}$  age of  $221.0 \pm 3.4$  Ma ( $1\sigma$ , MSWD = 2.0), which records a late Triassic W mineralization event in the Baishitouwa deposit. In combination with previous geochronological data, we suggest that NE China may have an enormous potential for Triassic W mineralization and more attention should be given to the Triassic ore prospecting in the region. This work highlights that the chemical composition of wolframite is controlled by both the crystallochemical parameters and the composition of the primary ore-forming fluid. Trace-element compositions suggest that wolframite (I) was controlled by the substitution mechanism of  $4^{\text{A}}(\text{Fe}, \text{Mn})^{2+} + 8^{\text{B}}\text{W}^{6+} + \text{B}\square \leftrightarrow 3^{\text{A}}\text{M}^{3+} + \text{A}\text{N}^{4+} + 7^{\text{B}}(\text{Nb}, \text{Ta})^{5+} + 2^{\text{B}}\text{N}^{4+}$ , whereas wolframite (II) was controlled by the substitution mechanism of  $^{\text{A}}(\text{Fe}, \text{Mn})^{2+} + \text{A}\square + 2^{\text{B}}\text{W}^{6+} \leftrightarrow 2^{\text{A}}\text{M}^{3+} + 2^{\text{B}}\text{N}^{4+}$ . Wolframite (I) contains higher concentrations of Nb, Ta, Sc, and heavy rare earth elements (HREEs), and lower Mn/(Mn + Fe) ratios than wolframite (II). Both wolframite (I) and (II) have similar trace elements and left-dipped REE<sub>N</sub> patterns, and analogical Nb/Ta ratios. They have similar Y/Ho ratios to Mesozoic highly fractionated W-mineralized granitoids in NE China. These data indicate that the W mineralization at Baishitouwa is genetically related to an underlying highly fractionated granite, and the compositional variation of fluids is likely driven by crystallization of wolframite during the processes of fluid evolution. A change of the ore-forming fluids from an oxidized to a relatively reduced state during the evolution occurred from stage 1 to 2.

**Keywords:** wolframite in situ U–Pb dating; wolframite geochemistry; hydrothermal W mineralization; Baishitouwa W deposit; NE China

## 1. Introduction

Most tungsten mineralization is spatially associated with highly evolved granites worldwide and form a large variety of deposit types, including quartz-vein, skarn, greisen, and porphyry-type [1–6]. Among these different mineralization styles, quartz–wolframite vein-type deposits provide approximately 44% of the world’s known economic tungsten

resource and contribute over 70% of the global tungsten production [7]. NE China, tectonically referred to as the Xing–Meng Orogenic Belt (XMOB), forms the eastern segment of the Central Asian Orogenic Belt and is one of the most important polymetallic metallogenic provinces in China [4,5,8–12] (Figure 1). More than 40 W deposits have been explored to date in this region [4,5]. These deposits have a combined total proven reserve of more than 0.62 Mt [5]. Based on the spatial distribution of these W deposits, three W belts can be identified, including the northern and central Great Xing’an Range W belt, southern Great Xing’an Range W belt (SGB), and Lesser Xing’an-Zhangguangcai Range W belt [5] (Figure 1c). Three episodes of W mineralization are identified, including Triassic (240–250 Ma), Early–Middle Jurassic (170–200 Ma), and Late Jurassic–Early Cretaceous (125–160 Ma) [5]. Previous studies mainly focused on the Jurassic and Early Cretaceous W mineralization [13–30]. In contrast, only a limited amount of research has been conducted on the Triassic deposits, especially the quartz–wolframite vein-type deposits [31,32], which hinders our understanding of regional W mineralization. In addition, previous studies on the ore genesis of quartz–wolframite vein-type deposits in this region were focused mainly on the geological features [33,34], geochronology of related granites [15,19,30,35], fluid inclusions [24,25,36], and isotopic analyses [13,18,21,23,26,29]. In contrast, wolframite, as the most important tungsten-bearing mineral in quartz–wolframite vein-type deposits, has not attracted the attention of researchers for many years, thus hindering our understanding of the detailed ore-forming process of quartz–wolframite vein-type deposits.

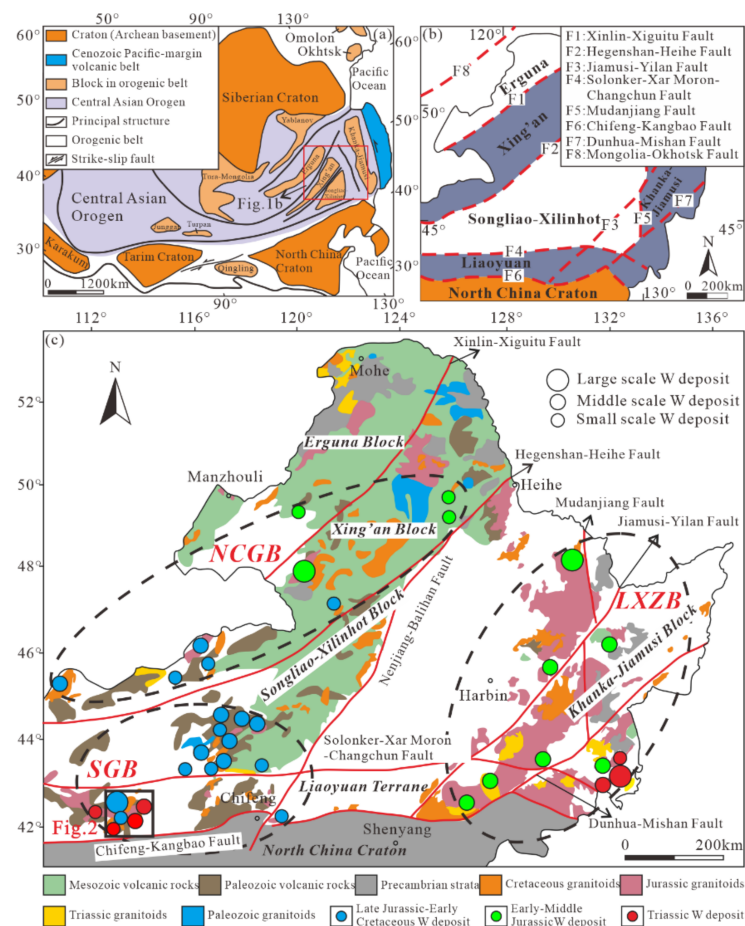


**Figure 1.** (a) Simplified tectonic map of the Central Asian Orogenic Belt (modified from [37]). (b) Schematic tectonic map of NE China (modified from [38]). (c) Distribution of major tungsten deposits in NE China (modified from [8]). Abbreviations are as follows: NCGB = the northern and central Great Xing’an Range W belt; SGB = the southern Great Xing’an Range W belt; LXZB = the Lesser Xing’an-Zhangguangcai Range W belt.

Accurate isotopic dating of hydrothermal minerals is a vital tool for constraining the timing of hydrothermal activity relative to intrusive magmatism, which is critical for constructing genetic models for hydrothermal deposits [39]. Zircons from spatially related granitic plutons are often used for U-Pb dating to constrain the formation age of W deposits [20,21,40,41]. However, these results are generally built upon a hypothesis that the dated granitic plutons are genetically related to W mineralization, which needs to be proved. Recent development in in situ U-Pb dating of wolframite provides an efficient approach to directly confine the timing of W mineralization and has been widely applied to quartz–wolframite vein-type deposits worldwide [40,42–46]. Electron probe microanalysis (EPMA) and laser ablation-inductively coupled plasma-mass spectrometry (LA-ICP-MS) in situ trace-element analysis has been used in many studies of mineral formation environments and mineralization processes [47–54]. Wolframite is the dominant tungsten mineral in quartz–wolframite vein-type deposits, which can incorporate significant amounts of Nb, Ta, rare earth elements (REEs), and other trace elements [55,56]. Numerous studies demonstrated that the trace elements and their variations in wolframite can record the physicochemical conditions and compositions of ore-forming fluids, thereby reflecting their source and evolution [1,56–59]. Although some studies have been conducted on the substitution mechanism of trace elements in wolframite, these studies commonly take different generations of wolframite as a whole without considering the possible differences between them [1,42]. The ambiguity has impeded the understanding of the ore-forming process of multi-stage quartz–wolframite vein-type deposits and can be potentially resolved by coupling detailed mineralogical observation and geochemical interpretation as shown in this study.

The Baishitouwa deposit, situated in the SGB, is a typical medium-scale quartz–wolframite vein-type deposit (Figures 1c and 2). Previous studies mainly focused on its geological characteristics [60] and petrogenesis [61]. The deposit represents an important Triassic hydrothermal W mineralization event and provides an excellent opportunity to investigate the mineralization mechanism. In this contribution, we identified two generations of wolframite based on extensive field observations and mineralogical thin-section observations. High-quality in situ U-Pb age of hydrothermal wolframite for the Baishitouwa deposit is presented, precisely pinning a Late Triassic W mineralization event in this region. Furthermore, in situ geochemical data of the two generations of wolframite are acquired to determine the substitution mechanism controlling the trace-element compositions of wolframite. The two generations of wolframite geochemistry also provide important information on the source and evolution of the ore-forming fluids. This paper improved our understanding of the regional W mineralization in NE China, as well as brought new insight into the origin and processes of tungsten mineralization of quartz–wolframite vein-type deposits.

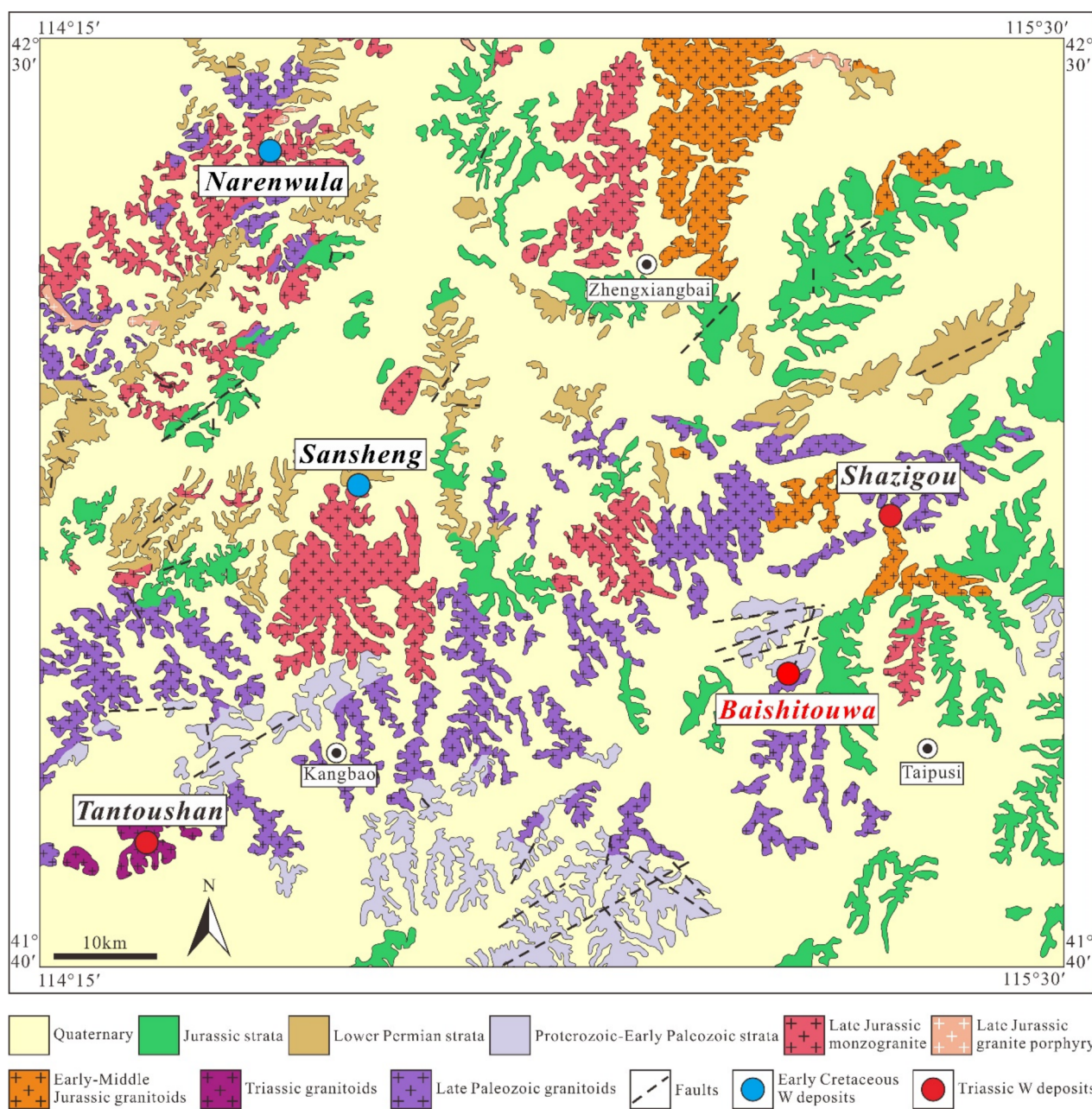


Figure 2. Schematic regional geological map of the Baishitouwa W deposit (after [62]).

## 2. Regional Geology

The tectonic components of the XMOB are composed of the Erguna Block, Xing’an Block, Songliao-Xilinhot Block, and Khanka-Jiamusi Block from NW to SE, and Liaoyuan Terrane in the south [37,38] (Figure 1). These tectonic components are separated by major faults, including the Xinlin–Xiguitu Fault, the Hegenshan–Heihe Fault, the Mudanjiang Fault, and the Solonker–Xar Moron–Changchun Fault (SXCF) [37,38] (Figure 1). The tectonic evolution of the area was closely related to the Paleo–Asian Ocean (PAO) regime during the Paleozoic to Early Mesozoic, which led to the amalgamation of several microcontinental blocks and the formation of multiarc systems and accretionary complexes [38,63–68]. Scissor-type closure of the PAO occurred during the Late Permian–Middle Triassic period along the SXCF, followed by a soft collision between the North China Craton and Siberian Craton [69–72]. From the Late Triassic onward, the tectonic framework of the XMOB was dominated by the closure of the Mongol–Okhotsk Ocean in the northwest, and subduction

of the Paleo-Pacific Ocean in the east [38,73–78]. During and after the longlived accretionary orogenic amalgamation and collision, the XMOB experienced a series of orogenic activity, back-arc basin formation, and extensive magmatism and mineralization [4,5,8–10,30,38,69,78–80].

The Narenwula–Baishitouwa W ore district, located in the southwestern part of the SGB (Figure 1c), hosts a series of quartz–wolframite vein-type deposits (i.e., Narenwula, Baishitouwa, Shazigou, and Tantoushan) and Sansheng porphyry W–Mo deposit (Figure 2). The region mainly contains units of Proterozoic–Early Paleozoic, Lower Permian, and Jurassic strata [62]. The Proterozoic–Early Paleozoic strata consists of leptite, granulite, quartzite, slate, phyllite, schist, and marble. The widely exposed Lower Permian and Jurassic strata comprise intermediate-acid volcanic rocks, volcanoclastic rocks, and sedimentary clastic rocks [62]. Four periods of granitic magmatism were identified, including Late Permian, Triassic, Early–Middle Jurassic, and Late Jurassic (Figure 2). The widespread Late Permian granodiorites and quartz diorites intrude into the Proterozoic–Early Palaeozoic strata. A Triassic granitic pluton is locally exposed in the southwestern part of this district. Early–Middle Jurassic fine-grained and minor biotite granites are mainly exposed in the western part of the district, along with minor occurrences in the eastern part. Late Jurassic monzogranites and granite porphyries are mainly exposed in the central and western parts of this district [62].

### 3. Ore Deposit Geology

The Baishitouwa W deposit is situated 16 km northwest of Taipusi Banner at 115°07' E, 41°56' E (Figure 2). The deposit has estimated reserves of 39,800 t WO<sub>3</sub> with a grade of 0.489% [81], and occurs within the mica schist of the Mesoproterozoic Baiyunebo Group (Figure 3). Faults in the mining district include NEE-, NW-, and NE-trending faults, with the NE-trending faults being the main ore-controlling structures (Figure 3a,b). An early Cretaceous granite pluton is exposed in the eastern part of the mining district, intruding the upper Jurassic Zhangjiakou Formation [61].

Seven ore bodies (Nos. 1, 2, 3, 4, 5, 6, and 7) are recognized for this deposit, of which No. 2 is the largest. The Nos. 1 and 2 ore bodies are exposed on the surface, and other ore bodies are concealed and controlled by drill holes (Figure 3b–d). The No. 1 ore body is controlled by NE-trending faults, with a length of approximately 128 m and an average thickness of 2.01 m. This ore body is dipping at an angle of 70–75° toward 305°. The No. 2 ore body is parallel to the No. 1 ore body, and occurs in the level at an altitude of 1276–1520 m. This ore body is 207 m in length, 0.47–4.42 m in thickness, and 77–260 m in depth. This ore body dips at an angle of 70–74° toward 300°. The No. 3 ore body dips at an angle of 74° toward 300°, with a depth of 178–335 m, a length of 181 m, and an average thickness of 1.81 m. The No. 4 ore body is 196 m in length, 1.42–4.20 m in thickness, and 259–392 m in depth. This ore body dips at an angle of 72–75° toward 325°. The No. 5 ore body dips at an angle of 73° toward 315°, with a depth of 1195–1220 m, a length of approximately 40 m, and an average thickness of 4.25 m. The No. 6 ore body is controlled by NE-trending faults, with a length of approximately 40 m and an average thickness of 9.01 m. This ore body dips at an angle of 75° toward 315°. The No. 7 ore body is 30 m in length and 2.53–3.78 m in thickness. This ore body dips at an angle of 73° toward 315°. The orebodies are mainly strata-bound or lenticular as revealed by borehole data and mapping of mine sections (Figure 3c,d).

The ores are mainly veined, massive, or disseminated (Figure 4). The main ore minerals are wolframite, pyrite, chalcopyrite, sphalerite, and galena (Figures 4 and 5). The gangue minerals are quartz, mica, sericite, chlorite, epidote, fluorite, and calcite (Figure 6). Wolframite is the main economic mineral in the Baishitouwa deposit and can be subdivided into two generations. Wolframite (I) commonly occurs as tabular, lath-shaped, columnar, and irregular crystals in fine-grained quartz–wolframite veins (Figure 4a,b and Figure 5a,b). Wolframite (II) is disseminated widely in interstices of the quartz grains (Figure 4c). A small amount of wolframite (II) is distributed in the quartz veins in leaf-like and scale-like forms, and coexists with coarse-grained prismatic quartz (Figure 4d). The

wolframite (II) is predominantly euhedral, tabular, and fine- to medium-grained, and coexists with pyrite and chalcopyrite (Figure 5c,d). The pyrite is euhedral to subhedral crystals, with sizes from 0.05 to 3 mm. Fine- and medium-grained pyrite is commonly replaced by sphalerite, galena, and chalcopyrite along the fractures and crystal margins (Figure 5c,d,h,i). The sphalerite is medium- to coarse-grained with an ir-regular shape, and often coexists with galena, pyrite, and chalcopyrite (Figure 5f,h,i). Exsolution textures of sphalerite–chalcopyrite solid solution are common, suggesting that they formed simultaneously (Figure 5f). The chalcopyrite is fine- to medium-grained with ir-regular shape and coexists with sphalerite, galena, and pyrite. The chalcopyrite can be subdivided into two types: the early generation of chalcopyrite is fine-grained and often forms an exsolution texture with sphalerite (Figure 5f), whereas the late generation of chalcopyrite is medium-grained and commonly replaces sphalerite, galena, and pyrite along the fractures and crystal margins (Figure 5f,i). The galena is fine- to medium-grained anhedral crystals and coexists with sphalerite, chalcopyrite, and pyrite (Figure 5g,h).

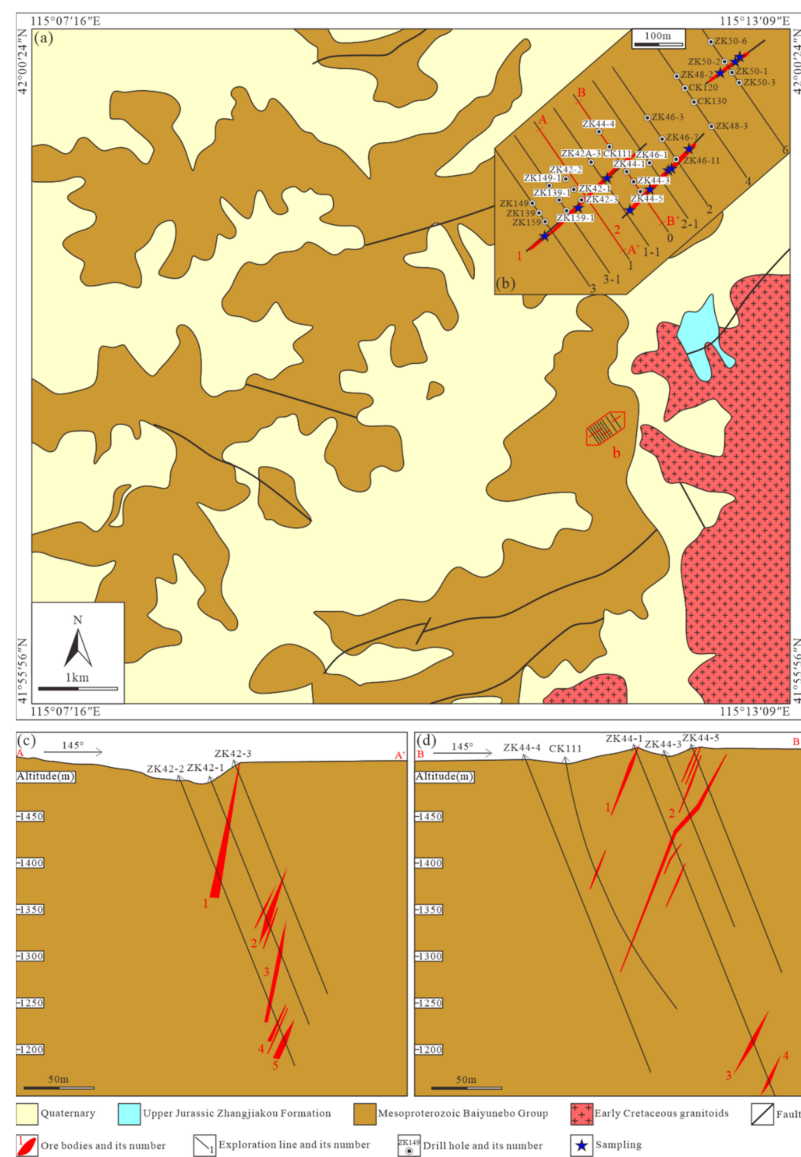


**Figure 3.** (a,b) Sketch geological maps of the Baishitouwa W polymetallic deposit. (c,d) Schematic geological cross section of No. 1 and No. 0 exploration line (after [81]).



**Figure 4.** Representative photographs of the mineralization at the Baishitouwa deposit. (a) Quartz–Wolframite (I) veins of stage 1 crosscut the country rocks (mica schist); (b) Quartz–Wolframite (I) ore of stage 1; (c) Quartz–Wolframite (II) ore of stage 2; (d) Quartz–Wolframite (II)–pyrite–chalcopyrite ore of stage 2; (e) Quartz–pyrite–chalcopyrite–sphalerite ore of stage 3; (f) Quartz–carbonate veins of stage 4. Abbreviations: Qtz, quartz; Wol (I), early generation of wolframite; Wol (II), late generation of wolframite; Py, pyrite; Ccp, chalcopyrite; Gn, galena; Sp, sphalerite; Car, carbonate.

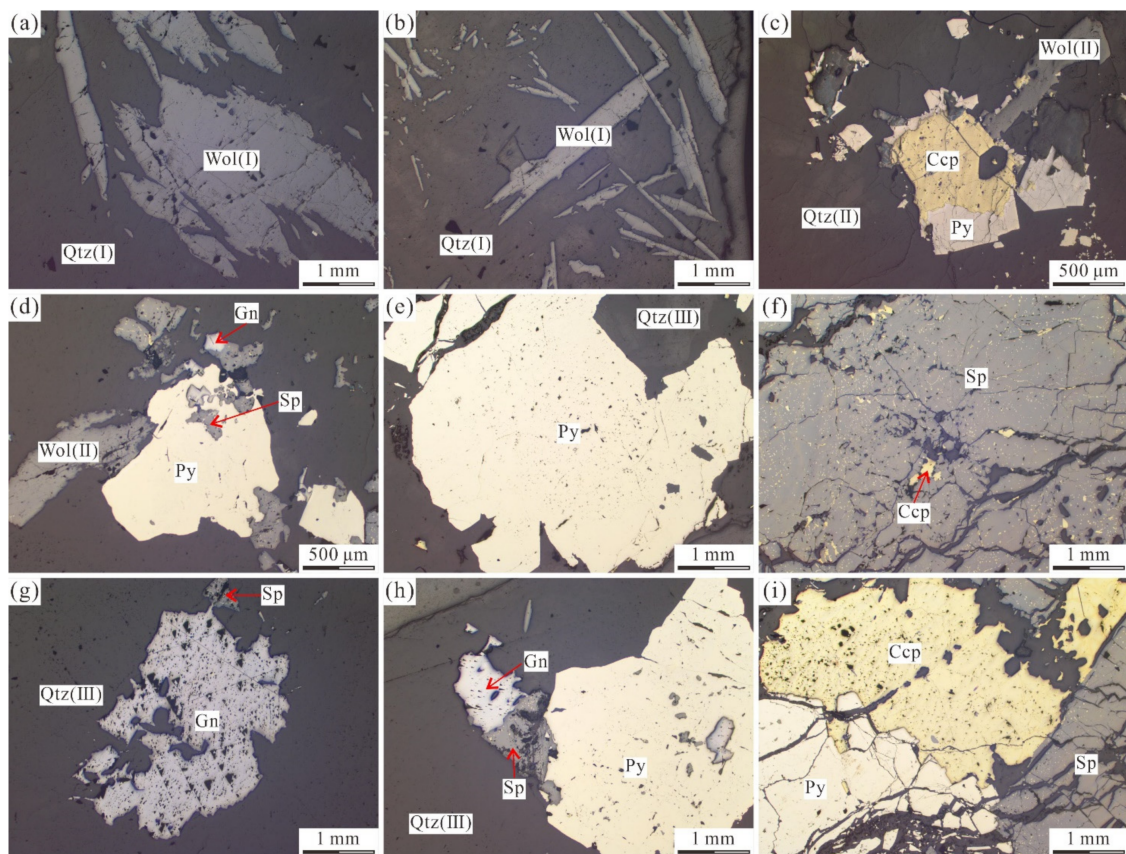


**Figure 5.** Representative photomicrographs of ore minerals from the Baishitouwa deposit. (a) Wolframite (I) intergrown with fine-grained quartz (<1 mm) of stage 1; (b) Wolframite (I) crystals occur as long columnar and needle columnar from stage 1; (c) Wolframite (II) coexisting with pyrite and chalcopyrite; (d) Wolframite (II) intergrown with pyrite of stage 2. Pyrite replaced by galena and sphalerite of stage 3 along fractures and crystal margins; (e) Medium-grained euhedral pyrite from stage 3; (f) The exsolution texture of sphalerite–chalcopyrite solid solution. Late generation of chalcopyrite replacing sphalerite along the fissure and margin; (g) Medium-grained anhedral galena and sphalerite intergrown with quartz from stage 3; (h) Sphalerite replacing pyrite along crystal margin, and galena replacing sphalerite and pyrite; (i) Late generation of chalcopyrite replacing pyrite and sphalerite along fractures and crystal margins. Abbreviations: Qtz, quartz; Wol (I), early generation of wolframite; Wol (II), late generation of wolframite; Py, pyrite; Ccp, chalcopyrite; Gn, galena; Sp, sphalerite.

Different types of alteration occurred in the Baishitouwa deposit, including silicification, sericitization, chloritization, epidotization, and carbonation (Figure 6). Silicification is observed as veins or as disseminations of quartz in ores or altered mica schist. Sericitization often occurs together with silicification, and is composed of sericite (Figure 6c–f). Chloritization and epidotization mainly consist of chlorite and epidote, respectively (Figure 6d–f). Carbonation is mainly composed of calcite, which represents the low-temperature alteration of the post-mineralization stage (Figure 4f).

Based on morphology, structure, mineralogy, and modes of occurrence, the hydrothermal ore-forming process of the Baishitouwa deposit can be divided into four stages: stage 1 of fine-grained quartz–wolframite (I), stage 2 of coarse-grained quartz–wolframite (II)–pyrite–chalcopyrite, stage 3 of quartz–polymetallic sulfides, and stage 4 of quartz–carbonate.

Stage 1 is the dominant W mineralization stage and is characterized by an assemblage of wolframite (I), quartz, and sericite. Abundant tabular crystals of wolframite (I) occur in fine-grained quartz–wolframite veins (Figure 4a,b). Wolframite (I) is medium- to coarse-

grained euhedral to subhedral crystals (Figure 5a,b). Sulfides are absent in this stage (Figure 4b). Stage 2 is characterized by an assemblage of wolframite (II), pyrite, chalcopyrite, quartz, and sericite. The quartz coexisting with wolframite (II) is coarse-grained pectinate or prismatic (Figure 4c,d). Wolframite (II) is disseminated widely in interstices of the quartz grains (Figure 4c), and small amounts of wolframite (II) are distributed in quartz veins in leaf- and scale-like forms (Figure 4d). Minor pyrite and chalcopyrite are present in this stage and intergrown with wolframite (II) (Figures 4d and 5c,d). Stage 3 is characterized by an assemblage of pyrite, chalcopyrite, galena, sphalerite, quartz, sericite, chlorite, and epidote. Abundant sulfides were formed in this stage. Pyrite is the most abundant sulfide, and is featured by medium- to coarse-grained euhedral to subhedral crystals (Figure 5e,h,i). However, the pyrite is commonly replaced by sphalerite, galena, and chalcopyrite along fractures and crystal margins (Figure 5h,i). Stage 4 is the final stage of the hydrothermal mineralization period in the Baishitouwa deposit. The veins from this stage are mainly composed of calcite and quartz (Figure 4f).

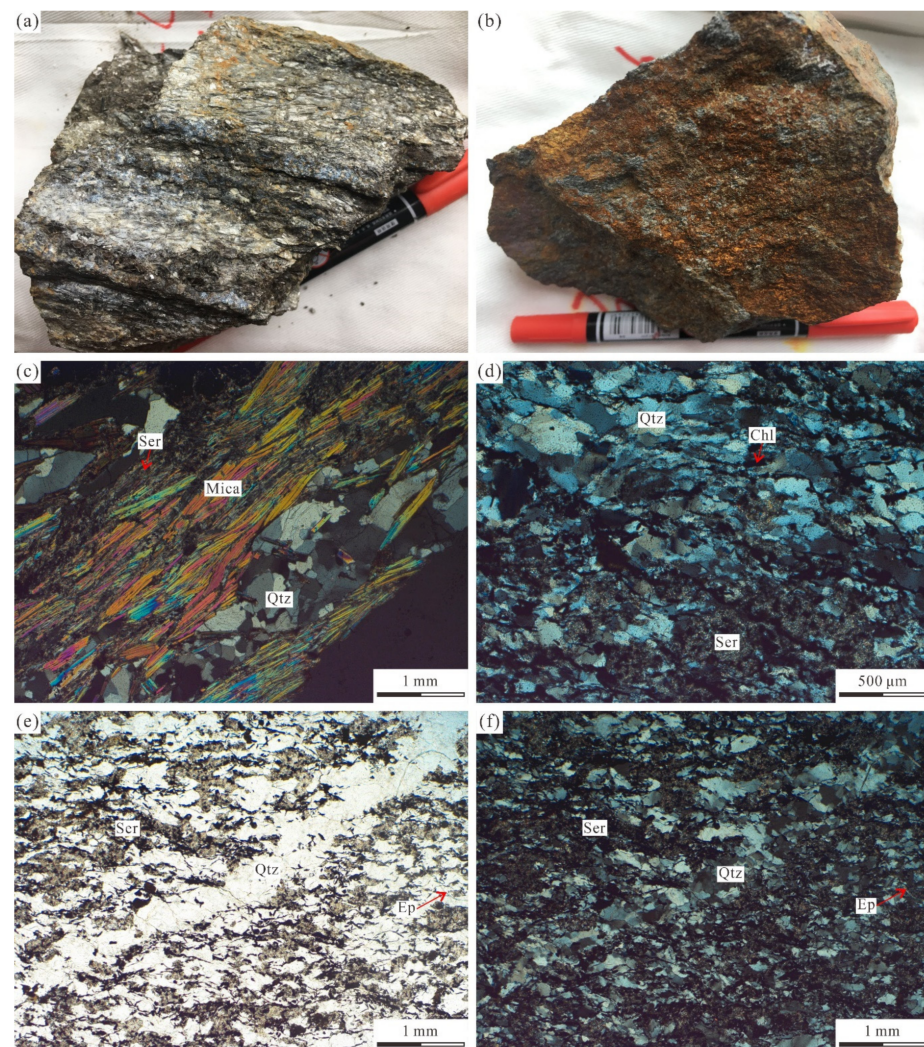


**Figure 6.** Representative hand specimen (a,b) and photomicrographs (c–f) of gangue minerals from the Baishitouwa deposit. (a,b) Mica schist. (c) Mica and quartz in mica schist. Sericitization (crossed-polarized light). (d) Silicification, chloritization, and sericitization (crossed-polarized light). (e) Silicification, epidotization, and sericitization (plane-polarized light). (f) Silicification, epidotization, and sericitization (crossed-polarized light). Abbreviations: Qtz, quartz; Ser, sericite; Chl, chlorite; Ep, epidote.

## 4. Sampling and Analytical Methods

### 4.1. Samples

The samples used for in situ U-Pb dating and geochemical analysis during this study were collected from Nos. 1 and 2 ore bodies' exposures within open pits. The sampling locations are shown in Figure 3b. Wolframite (I) samples (BST-9, BST-15, and BST-16) and wolframite (II) samples (BST-12, BST-29, and BST-30) were collected from quartz–wolframite (I) and quartz–wolframite (II)(–pyrite–chalcopyrite) veins of No. 1 ore body, respectively. Wolframite (I) samples (BST-17 and BST-38) and wolframite (II) samples (BST-26, BST-27, and BST-28) were collected from quartz–wolframite (I) and quartz–wolframite (II)(–pyrite–chalcopyrite) veins of No. 2 ore body, respectively. All the samples were prepared as polished probe sections for the microscopic observations of mineral assemblages. To better identify the internal wolframite textures and improve the reliability of the analytical data, backscattered electron images of wolframite samples were generated at the Key Laboratory of Mineral Resources, Institute of Geology and Geophysics, Chinese Academy of Sciences. Wolframite (I) sample BST-17 was used for laser ablation-inductively coupled plasma-mass spectrometry (LA-SF-ICP-MS) in situ U-Pb dating analyses. Wolframite (I) samples (BST-9, BST-15, BST-17, and BST-38) and wolframite (II) samples (BST-12 and BST-26) were selected for EPMA and LA-ICP-MS analyses. All wolframite zones selected for in situ geochemical analyses were free of internal zoning, micro-inclusions, replacement phases, exsolution evidence, and alteration features.

### 4.2. EPMA

EPMA of the wolframite samples was conducted at the Wuhan Sample Solution Analytical Technology Co., Ltd., Wuhan, China. Major- and trace-elemental composition of the wolframite were measured using a JEOL JXA 8230 EPMA equipped with five wavelengths dispersive X-ray (WDX) spectrometers. The operating conditions used a 15-kV acceleration voltage, a 50 nA beam current, and a 1  $\mu\text{m}$  beam diameter. Standards used for data correction were wolframite for W, hematite for Fe, manganite for Mn, and Nb metal for Nb. Spectral lines, peak times, and off-peak background times used for the WDS analyses were as follows: W ( $L\alpha$ , 10, 5), Fe ( $K\alpha$ , 10, 5), Mn ( $K\alpha$ , 10, 5), and Nb ( $L\alpha$ , 10, 5). The analytical uncertainties were 0.4 wt% for  $\text{WO}_3$ , 0.2 wt% for FeO, 0.1 wt% for MnO, and 0.05 wt% for  $\text{Nb}_2\text{O}_5$ . The detection limits for all of the analyzed elements were below 0.01 wt%.

### 4.3. LA-SF-ICP-MS U-Pb Dating

The samples were ablated using a GeoLasPro 193 nm ArF excimer laser (CompexPro 102F, Coherent) coupled with a Thermo Scientific Element XR sector field ICP-MS at the State Key Laboratory of Ore Deposit Geochemistry, Institute of Geochemistry, Chinese Academy of Sciences in Guiyang, China. A laser frequency of 6 Hz, an energy density of 5  $\text{J}/\text{cm}^2$ , and a spot size of 32  $\mu\text{m}$  was used for the analyses. Primary standard materials, YGX [44] and WT [82], were analyzed twice for every 15 analyses of the unknown samples. A detailed description of the analytical conditions and methods can be found in [43,83]. The ICP-MS data were processed offline using the ICPMSDataCal software for calibration, background correction, and floating of the integration signal [84]. No downhole corrections were made for only the first ~25 s of ablation data (excluding the initial ~2 s) used in the process. Isoplot 4.15 was used to calculate the U-Pb ages and generate Concordia diagrams. Common Pb corrections were employed using a Tera–Wasserburg Concordia or a Tera–Wasserburg Concordia anchored through common Pb [85]. The lower intercept ages were used as the timing of mineral precipitation of wolframite [85–87]. Data errors for the isotopic ratios in the following samples are 1  $\sigma$ .

### 4.4. LA-ICP-MS Analyses

LA-ICP-MS analyses were conducted at the Wuhan Sample Solution Analytical Technology Co., Ltd., Wuhan, China. Laser sampling was performed using a GeoLas2005

laser ablation system and an Agilent 7700e ICP-MS. The instrumental settings and operational procedures used herein were similar to those described in [56,88]. The laser ablation system was equipped with a signal-smoother to compensate for the low-frequency laser pulse [89]. The time-resolved signal included two intervals: the background (20–30 s) and the analytical signal (50 s). No internal standards were used, but multiple external standards [88] were applied to calculate the elemental concentrations. United States Geological Survey (USGS) reference glasses (e.g., BCR-2G, BIR-1G, and BHVO-2G) were used as the calibration standards [90]. The elemental concentrations of the USGS glasses can be found in the GeoReM database (<http://georem.mpch-mainz.gwdg.de/> accessed on 1 March 2022). The ICPMSDataCal software [84,88] was used for offline data processing, including analytical and background signal determinations, sensitivity drift calibrations, and elemental concentration calculations.

## 5. Results

### 5.1. Wolframite U-Pb Age

The U-Pb isotope data from the wolframite sample BST-17 are listed in Table 1. The uncorrected U-Pb data are plotted on a U-Pb Tera–Wasserburg diagram in Figure 7. Nineteen spot analyses of the wolframite sample had total Pb, Th, and U concentrations varying from 0.29 to 3.89 ppm, from 0.01 to 0.86 ppm, and from 1.65 to 127.46 ppm, respectively. A lower intercept  $^{206}\text{Pb}/^{238}\text{U}$  age of  $221.0 \pm 3.4$  Ma ( $1 \sigma$ , MSWD = 2.0) was obtained from the Tera–Wasserburg Concordia diagram (Figure 7).

### 5.2. In Situ Major and Trace-Element Compositions of Wolframite

The chemical compositions of wolframite from the Baishitouwa deposit determined using EPMA are listed in Table 2. The trace elements in the wolframite measured using LA-ICP-MS are listed in Table 3.

The wolframite had the following major elemental composition: wolframite (I) has higher FeO contents (3.83–6.74 wt%) and lower MnO contents (16.81–19.59 wt%) than wolframite (II) (FeO 1.83–3.59 wt%, MnO 19.58–21.23 wt%). Wolframite (I) and wolframite (II) were Mn-dominated with Mn/(Mn + Fe) values of 0.72–0.84 and 0.85–0.92, respectively (Figure 8a). It is clearly shown in Figure 8b that Mn and Fe contents correlate in the two generations of wolframite, and the data points are aligned along the 1:1 substitution line. A reliable anticorrelation ( $R^2 \approx 0.96$ ) is found between W + Nb and Fe + Mn for all samples with a low slope of  $-0.35$  (Figure 8c).

**Table 1.** LA-SF-ICP-MS U-Pb isotope data of the wolframite sample BST-17 from the Baishitouwa deposit.

Sample	Pb ppm	Th ppm	U ppm	$^{207}\text{Pb}/^{206}\text{Pb}$		$^{207}\text{Pb}/^{235}\text{U}$		$^{206}\text{Pb}/^{238}\text{U}$		Rho	$^{238}\text{U}/^{206}\text{Pb}$		$^{207}\text{Pb}/^{206}\text{Pb}$	
				Ratio	1sigma	Ratio	1sigma	Ratio	1sigma		Ratio	Percent	Ratio	Percent
BST-17-01	0.37	0.05	1.65	0.51803	0.04001	3.77648	0.96695	0.06225	0.00319	0.20019	13.976	5.126	0.518	7.724
BST-17-02	0.29	0.04	2.38	0.24036	0.02915	1.12194	0.29722	0.04172	0.00223	0.20131	20.852	5.333	0.240	12.126
BST-17-03	0.47	0.10	6.88	0.21636	0.02093	1.02506	0.27473	0.03649	0.00138	0.14159	23.840	3.795	0.216	9.676
BST-17-04	1.67	0.62	34.19	0.15633	0.00536	0.74706	0.18657	0.03541	0.00071	0.08024	24.570	2.004	0.156	3.427
BST-17-05	0.67	0.06	10.50	0.16506	0.01046	0.75614	0.19240	0.03523	0.00091	0.10120	24.693	2.575	0.165	6.337
BST-17-06	1.91	0.15	41.61	0.14327	0.00866	0.64880	0.16431	0.03427	0.00065	0.07456	25.386	1.888	0.143	6.048
BST-17-07	1.72	0.10	45.18	0.07509	0.00261	0.33590	0.08394	0.03297	0.00069	0.08389	26.392	2.096	0.075	3.477
BST-17-08	1.38	0.49	34.95	0.09940	0.00415	0.43514	0.10859	0.03282	0.00049	0.05986	26.508	1.494	0.099	4.171
BST-17-09	0.54	0.01	11.34	0.09650	0.00779	0.39049	0.09993	0.03260	0.00118	0.14101	26.686	3.609	0.097	8.072
BST-17-10	0.76	0.22	21.15	0.06575	0.00497	0.28654	0.07315	0.03257	0.00075	0.09047	26.713	2.310	0.066	7.562
BST-17-11	1.19	0.00	26.05	0.11695	0.00769	0.49424	0.12543	0.03236	0.00065	0.07924	26.889	2.011	0.117	6.578
BST-17-12	2.40	0.07	73.88	0.06423	0.00208	0.27825	0.06957	0.03154	0.00055	0.06992	27.584	1.748	0.064	3.245
BST-17-13	1.96	0.03	54.73	0.08372	0.00423	0.34614	0.08682	0.03120	0.00059	0.07522	27.883	1.887	0.084	5.055
BST-17-14	1.31	0.05	33.14	0.11018	0.00510	0.45949	0.11549	0.03115	0.00059	0.07584	27.930	1.906	0.110	4.632
BST-17-15	1.22	0.06	31.90	0.11501	0.00671	0.48401	0.12306	0.03110	0.00050	0.06274	27.974	1.595	0.115	5.832
BST-17-16	1.79	0.05	54.93	0.05652	0.00224	0.23706	0.05938	0.03091	0.00051	0.06623	28.147	1.659	0.057	3.958
BST-17-17	3.89	1.16	127.46	0.05613	0.00135	0.23652	0.05886	0.03074	0.00049	0.06437	28.301	1.602	0.056	2.401
BST-17-18	2.66	0.34	86.15	0.05859	0.00173	0.24287	0.06055	0.03028	0.00046	0.06129	28.730	1.528	0.059	2.953
BST-17-19	1.10	0.03	35.31	0.04911	0.00273	0.19797	0.04989	0.03010	0.00057	0.07477	28.902	1.884	0.049	5.563

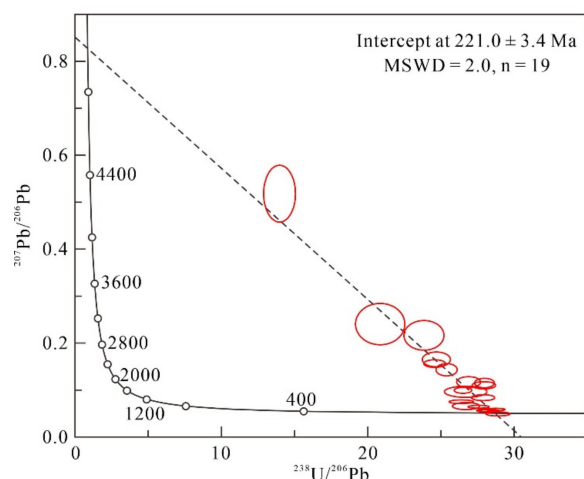


Figure 7. Tera–Wasserburg plots and the lower intercept’s age of wolframite sample BST-17 from the Baishitouwa deposit.

Wolframite from the Baishitouwa deposit has been characterized by variable trace-elemental compositions (Figure 9). In wolframite (I) samples, concentrations above 10 ppm were observed for six elements (Table 3): Sc (46.32–57.43 ppm, median 50.67 ppm), Ti (159.61–433.26 ppm, median 239.03 ppm), Zr (55.73–64.32 ppm, median 59.51 ppm), Nb (94.35–165.00 ppm, median 117.58 ppm), Sn (9.10–25.75 ppm, median 13.70 ppm), and Zn (11.54–14.33 ppm, median 12.54 ppm). V, Y, Hf, U, Dy, Er, Yb, and Lu concentrations ranged from 1 to 10 ppm, whereas the other elemental concentrations were less than 1 ppm. In wolframite (II) samples, concentrations above 10 ppm were observed for five elements: Sc (21.78–34.24 ppm, median 27.70 ppm), Ti (352.02–1093.89 ppm, median 663.62 ppm), Zr (17.89–31.40 ppm, median 21.67 ppm), Nb (7.46–16.86 ppm, median 13.42 ppm), Sn (34.70–129.92 ppm, median 59.87 ppm). V, Cr, Zn, U, and Yb concentrations were varying from 1 to 10 ppm, whereas the other elemental concentrations were less than 1 ppm. The Hg concentration was mainly below the detection limit (Table 3). The concentrations of Nb, Ta, Sc, Zr, Hf, Pb, and Eu in wolframite (I) are higher than those in wolframite (II), whereas the concentrations of Ti, Sn, Cr, and Th in wolframite (I) are lower than those in wolframite (II) (Figure 9).

Table 2. Chemical composition of wolframite by EPMA (in wt%).

Sample	Stage	Nb <sub>2</sub> O <sub>5</sub>	WO <sub>3</sub>	FeO	MnO	Total	Nb (apfu)	W (apfu)	Fe (apfu)	Mn (apfu)	Mn/(Mn + Fe)
BST-9-01	1	0.11	76.42	4.17	18.83	99.55	0.0025	1.0029	0.1766	0.8075	0.18
BST-9-02	1	0.11	76.15	4.68	18.18	99.14	0.0026	1.0034	0.1988	0.7826	0.20
BST-9-03	1	0.08	76.19	3.93	18.76	98.98	0.0019	1.0060	0.1674	0.8095	0.17
BST-9-04	1	0.03	75.96	4.68	18.48	99.17	0.0008	1.0008	0.1991	0.7955	0.20
BST-15-01	1	0.04	76.01	4.03	19.35	99.44	0.0010	0.9985	0.1708	0.8307	0.17
BST-15-02	1	0.12	76.43	5.32	18.02	99.91	0.0027	0.9993	0.2245	0.7698	0.23
BST-15-03	1	0.01	76.23	5.00	18.18	99.43	0.0003	1.0020	0.2120	0.7809	0.21
BST-15-04	1	0.00	76.43	3.86	19.17	99.53	0.0000	1.0034	0.1634	0.8224	0.17
BST-15-05	1	0.09	76.06	4.66	18.61	99.46	0.0020	0.9989	0.1976	0.7984	0.20
BST-17-01	1	0.08	76.81	4.51	18.74	100.13	0.0018	1.0023	0.1897	0.7989	0.19
BST-17-02	1	0.04	76.47	4.87	18.48	99.89	0.0009	1.0001	0.2053	0.7898	0.21
BST-17-03	1	0.00	77.34	3.85	19.59	100.78	0.0000	1.0029	0.1610	0.8299	0.16
BST-17-04	1	0.11	76.94	3.88	19.28	100.22	0.0024	1.0029	0.1630	0.8211	0.17
BST-17-05	1	0.01	76.44	4.01	19.40	99.92	0.0002	0.9993	0.1693	0.8286	0.17
BST-17-06	1	0.09	76.34	3.83	19.35	99.61	0.0019	1.0012	0.1622	0.8290	0.16
BST-38-01	1	0.01	76.62	6.30	17.19	100.14	0.0003	0.9999	0.2653	0.7331	0.27
BST-38-02	1	0.00	76.97	6.74	16.81	100.52	0.0000	1.0008	0.2829	0.7142	0.28
BST-38-03	1	0.00	76.29	6.15	17.07	99.54	0.0000	1.0017	0.2607	0.7322	0.26
BST-38-04	1	0.00	77.12	6.15	17.38	100.65	0.0000	1.0016	0.2578	0.7375	0.26
BST-38-05	1	0.08	76.96	6.19	16.99	100.23	0.0018	1.0034	0.2604	0.7237	0.26
BST-12-01	2	0.14	76.23	3.59	19.58	99.58	0.0031	0.9996	0.1520	0.8388	0.15
BST-12-02	2	0.00	76.28	1.83	21.23	99.35	0.0001	1.0032	0.0777	0.9125	0.08
BST-26-01	2	0.05	77.07	2.43	20.71	100.29	0.0012	1.0039	0.1022	0.8813	0.10
BST-26-02	2	0.00	76.57	2.76	20.47	99.86	0.0000	1.0017	0.1164	0.8750	0.12
BST-26-03	2	0.00	77.19	2.55	20.84	100.57	0.0000	1.0028	0.1068	0.8845	0.11
BST-26-04	2	0.03	76.46	2.27	21.10	99.88	0.0007	1.0000	0.0959	0.9018	0.10
BST-26-05	2	0.01	76.62	2.19	21.22	100.11	0.0003	0.9996	0.0922	0.9044	0.09

Table 3. Chemical composition of wolframite by LA-ICP-MS (in ppm).

Spots Stage	BST-9-01 1	BST-9-02 1	BST-15-01 1	BST-15-02 1	BST-17-01 1	BST-17-02 1	BST-17-03 1	BST-38-01 1	BST-38-02 1	
Mg	60.31	60.31	60.31	60.31	60.31	60.31	60.31	60.31	60.31	
Li	0.3493	0.2195	0.4646	0.5704	0.4218	0.4236	0.4856	0.2971	0.6629	
Be	0.0448	0.0888	<LOD	0.0888	<LOD	<LOD	0.0448	0.1325	0.1328	
B	<LOD	0.4653	0.2412	<LOD	<LOD	0.1205	<LOD	0.2397	0.9252	
Sc	57.43	49.08	49.94	50.67	51.45	49.36	46.32	50.91	53.53	
Ti	433.26	213.28	230.42	229.58	276.46	239.03	159.61	330.02	339.64	
V	7.98	5.42	5.51	6.55	6.70	5.28	5.23	5.83	6.51	
Cr	0.1013	0.1356	0.1475	0.1206	0.1169	0.1023	0.2584	0.3059	0.4237	
Co	0.0502	0.0356	0.0062	<LOD	0.0421	0.0663	0.0460	<LOD	0.0488	
Ni	0.2836	0.3975	<LOD	0.0552	0.4265	0.2570	0.6007	<LOD	<LOD	
Cu	<LOD	<LOD	0.0578	0.1247	0.0391	<LOD	<LOD	0.1309	0.0305	
Zn	13.30	11.82	12.15	11.54	14.33	12.54	14.31	12.35	13.03	
Ga	1.04	1.20	0.99	1.11	0.77	1.36	0.82	0.61	0.72	
Rb	0.07	0.03	0.01	<LOD	<LOD	0.08	<LOD	0.05	0.13	
Sr	0.15	0.01	0.16	0.01	0.17	0.13	0.12	0.01	0.01	
Y	3.27	2.89	2.69	2.78	3.10	2.75	2.76	2.92	3.01	
Zr	64.14	56.42	59.51	58.27	60.73	55.95	55.73	60.93	64.32	
Nb	165.00	94.35	140.33	106.03	117.58	105.49	95.47	127.74	156.00	
Mo	0.0247	0.0246	<LOD	0.0492	0.0016	0.0249	0.0248	0.0245	<LOD	
Ag	0.0078	0.0117	0.0064	0.0111	0.0060	0.0145	<LOD	0.0056	0.0175	
Cd	0.3384	0.2233	0.0566	<LOD	0.1685	<LOD	0.0559	0.0550	<LOD	
Sn	25.75	11.38	13.70	12.71	14.49	12.66	9.10	17.47	21.24	
Sb	<LOD	<LOD	0.0758	<LOD	0.0437	0.0036	<LOD	<LOD	<LOD	
Cs	0.0120	0.0052	0.0111	<LOD	0.0012	0.0306	0.0254	0.0098	0.0914	
Ba	0.2443	0.0860	0.0200	0.0345	0.0208	0.0525	0.0523	0.0011	0.0518	
La	0.0020	<LOD	0.0103	0.0020	<LOD	0.0021	0.0021	0.0082	0.0062	
Ce	<LOD	0.0113	0.0027	0.0021	0.0064	0.0046	0.0064	<LOD	<LOD	
Pr	<LOD	0.0053	0.0003	0.0018	0.0054	<LOD	<LOD	0.0018	0.0018	
Nd	0.0238	<LOD	0.0125	0.0431	<LOD	0.0219	0.0231	0.0108	0.0218	
Sm	0.0100	0.0368	0.0285	0.0247	0.0125	0.0251	0.0139	0.0497	0.0138	
Eu	0.0311	0.0500	0.0377	0.0342	0.0377	0.0189	0.0600	0.0500	0.0700	
Gd	0.2565	0.1883	0.1367	0.2001	0.1470	0.1483	0.1500	0.0674	0.1785	
Tb	0.1108	0.1098	0.0903	0.1353	0.1137	0.0853	0.0800	0.1126	0.0862	
Dy	1.48	1.35	1.17	1.36	1.19	1.36	1.19	1.42	1.32	
Ho	0.44	0.43	0.38	0.42	0.44	0.40	0.32	0.38	0.36	
Er	2.03	1.82	1.70	1.79	1.89	1.59	1.82	1.76	2.18	
Tm	0.54	0.49	0.46	0.53	0.52	0.46	0.49	0.48	0.44	
Yb	5.80	5.12	5.20	5.45	5.16	4.90	4.58	4.92	4.80	
Lu	1.25	1.08	1.06	0.97	1.08	0.94	1.06	1.04	1.08	
ΣREE	11.95	10.64	10.46	10.77	10.79	9.79	9.75	10.28	10.49	
LREE	0.06	0.08	0.09	0.11	0.06	0.07	0.06	0.09	0.05	
HREE	11.89	10.56	10.37	10.67	10.72	9.71	9.69	10.19	10.43	
Hf	1.25	1.17	1.10	1.14	1.09	0.94	0.83	0.88	1.22	
Ta	1.20	0.61	1.15	0.68	0.78	0.58	0.59	1.01	1.15	
Hg	<LOD									
Pb	0.4451	0.4087	0.1899	0.1861	0.1772	0.1287	0.1134	0.0849	0.0629	
Th	0.0471	0.0357	0.0393	0.0362	0.0025	0.0894	0.0629	0.0555	0.0762	
U	12.72	5.54	6.13	5.92	7.89	6.60	4.05	8.82	9.53	
Zr/Hf	51.45	48.31	53.96	51.02	55.78	59.63	67.29	69.36	52.71	
Y/Ho	7.51	6.70	7.02	6.62	7.08	6.90	8.57	7.76	8.47	
Nb/Ta	137.33	155.44	121.76	156.97	151.61	182.58	163.15	126.16	135.48	
Spots Stage	BST-12-01 2	BST-12-02 2	BST-12-03 2	BST-12-04 2	BST-12-05 2	BST-26-01 2	BST-26-02 2	BST-26-03 2	BST-26-04 2	BST-26-05 2
Mg	60.31	60.31	60.31	60.31	60.31	60.31	60.31	60.31	60.31	60.31
Li	<LOD	0.0884	<LOD	0.0045	0.2520	0.0593	0.4895	0.5664	0.5126	0.3248
Be	<LOD	0.0598	0.1014	<LOD	<LOD	0.0562	0.0685	0.2707	<LOD	0.2472
B	0.0207	<LOD	1.7015	1.1804	<LOD	0.6596	1.3580	1.2912	<LOD	0.5255
Sc	30.72	23.51	27.97	27.43	23.03	21.78	23.64	28.01	31.06	34.24
Ti	726.15	586.84	705.13	625.26	552.80	967.20	434.20	352.02	701.97	1093.89
V	7.83	7.29	8.78	7.21	6.76	10.70	3.85	4.45	8.43	11.44
Cr	0.4404	0.5152	0.5756	0.5777	0.6714	0.7117	0.8770	0.9870	4.1304	20.1160
Co	0.0767	0.0819	0.1016	0.0651	0.1021	0.0684	<LOD	<LOD	0.0127	0.0702
Ni	<LOD	<LOD	0.4152	0.3080	0.4783	0.5693	<LOD	0.9805	0.3265	0.3592
Cu	<LOD	<LOD	<LOD	<LOD	0.3566	0.0067	0.0535	4.1115	0.0969	5.2102
Zn	6.51	7.19	8.36	7.24	8.36	8.35	6.81	7.65	7.81	12.22
Ga	1.10	0.90	1.10	0.80	0.62	1.49	0.55	1.30	0.93	1.39
Rb	0.02	0.03	<LOD	<LOD	0.04	<LOD	0.03	0.02	<LOD	0.10
Sr	0.02	0.27	0.28	0.04	0.02	0.62	0.13	0.94	0.38	1.09
Y	1.38	0.96	1.22	1.19	1.19	1.45	1.25	1.46	1.80	2.35
Zr	22.47	20.27	21.81	21.52	18.09	21.87	17.89	21.43	25.89	31.40
Nb	16.09	8.55	11.00	10.56	13.62	14.85	16.53	16.86	13.22	7.46
Mo	0.0519	0.0259	0.0259	<LOD	0.0519	0.0255	<LOD	<LOD	<LOD	0.1180
Ag	<LOD	<LOD	0.0008	<LOD	0.0438	0.0013	<LOD	0.0292	<LOD	<LOD
Cd	0.1153	0.1162	0.1165	0.0675	<LOD	0.2343	0.1214	2.2250	0.1210	2.7041
Sn	54.79	50.35	73.35	64.94	34.70	109.22	34.95	50.08	79.12	129.92
Sb	0.0278	0.0521	0.1070	0.0076	<LOD	0.0892	<LOD	<LOD	0.1238	<LOD
Cs	<LOD	0.0634	0.0016	<LOD	<LOD	0.0087	<LOD	0.0760	0.0281	0.0191
Ba	0.0176	0.0397	0.2206	<LOD	<LOD	0.1987	0.0292	5.5505	0.2333	5.1689
La	0.0063	0.0131	0.0087	<LOD	<LOD	0.0069	0.0058	0.0051	0.0191	0.0102
Ce	0.0024	0.0115	0.0024	0.0073	<LOD	0.0397	0.0178	0.0169	0.0087	0.0256

Table 3. Cont.

Spots Stage	BST-12-01 2	BST-12-02 2	BST-12-03 2	BST-12-04 2	BST-12-05 2	BST-26-01 2	BST-26-02 2	BST-26-03 2	BST-26-04 2	BST-26-05 2
Pr	0.0020	0.0057	<LOD	<LOD	<LOD	0.0040	0.0003	0.0020	0.0143	0.0002
Nd	0.0673	0.0252	0.0238	0.0116	0.0116	0.0455	0.0149	0.0440	<LOD	0.0141
Sm	0.0265	0.0266	0.0265	0.0134	0.0133	0.0657	0.0100	0.0343	0.0017	0.0594
Eu	0.0100	0.0132	0.0100	0.0133	0.0069	0.0168	0.0139	0.0100	0.0180	0.0239
Gd	0.0463	0.0761	0.1195	0.0052	0.0849	0.0828	<LOD	<LOD	0.0335	0.0428
Tb	0.0298	0.0252	0.0250	0.0391	0.0328	0.0265	0.0256	0.0161	0.0511	0.0507
Dy	0.43	0.26	0.46	0.31	0.43	0.46	0.44	0.23	0.46	0.54
Ho	0.10	0.08	0.10	0.11	0.14	0.14	0.08	0.08	0.15	0.17
Er	0.55	0.41	0.62	0.54	0.56	0.63	0.57	0.50	0.67	0.76
Tm	0.16	0.12	0.13	0.14	0.13	0.12	0.12	0.16	0.17	0.17
Yb	1.58	1.29	1.28	1.48	1.44	1.45	1.35	1.65	2.01	2.42
Lu	0.33	0.23	0.26	0.31	0.31	0.29	0.34	0.31	0.38	0.55
ΣREE	3.33	2.59	3.05	2.98	3.17	3.38	2.97	3.05	3.99	4.83
LREE	0.10	0.10	0.06	0.05	0.03	0.18	0.05	0.10	0.06	0.13
HREE	3.23	2.50	2.99	2.94	3.13	3.20	2.91	2.95	3.93	4.70
Hf	0.33	0.28	0.28	0.17	0.11	0.22	0.13	0.08	0.33	0.48
Ta	0.11	0.09	0.08	0.07	0.09	0.09	0.16	0.18	0.17	0.10
Hg	<LOD									
Pb	0.0566	0.0449	0.0420	0.0400	0.0389	0.0244	0.0218	0.0164	0.0050	0.0119
Th	0.0533	0.2093	0.1500	0.0949	0.0860	0.3668	0.1626	0.2699	0.5558	0.5835
U	6.29	3.59	8.19	4.86	2.82	9.74	7.17	8.75	15.22	18.62
Zr/Hf	68.82	71.45	76.80	128.41	165.89	98.36	139.61	253.61	78.21	65.68
Y/Ho	13.30	11.69	12.18	11.01	8.34	10.57	15.44	18.97	12.03	13.82
Nb/Ta	149.93	97.51	132.65	149.55	154.31	158.27	103.31	94.49	77.65	76.91

LOD = Limits of detection.

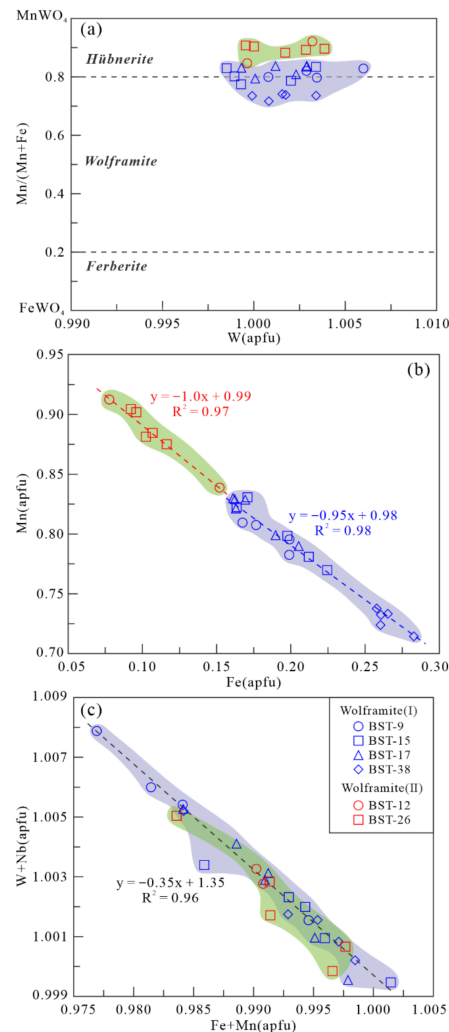
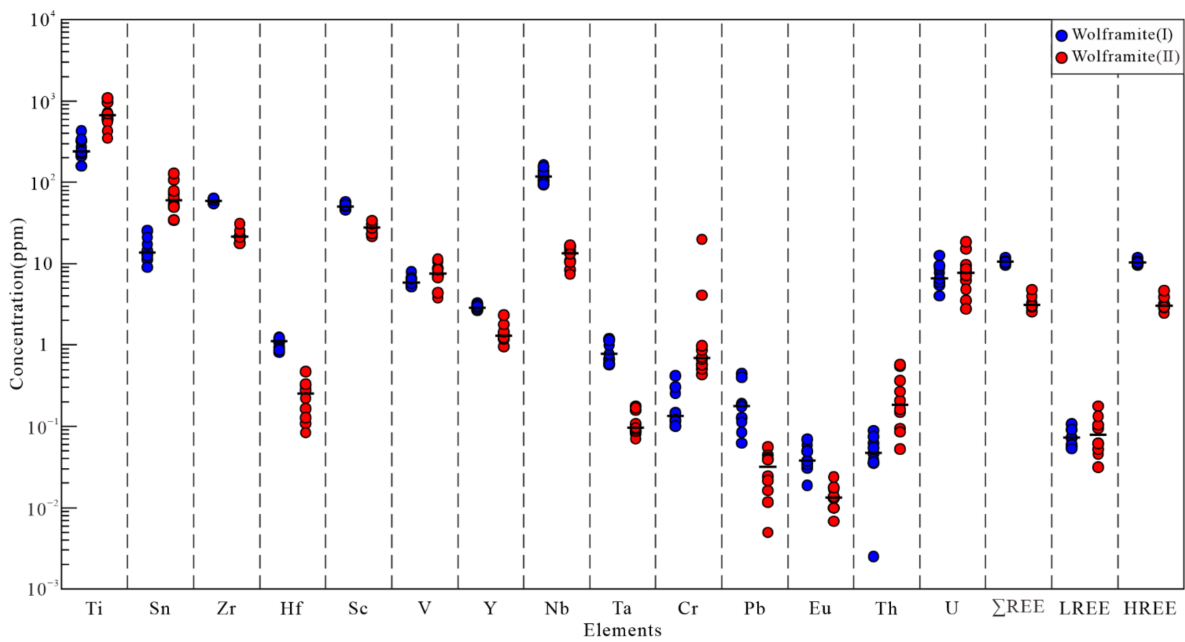
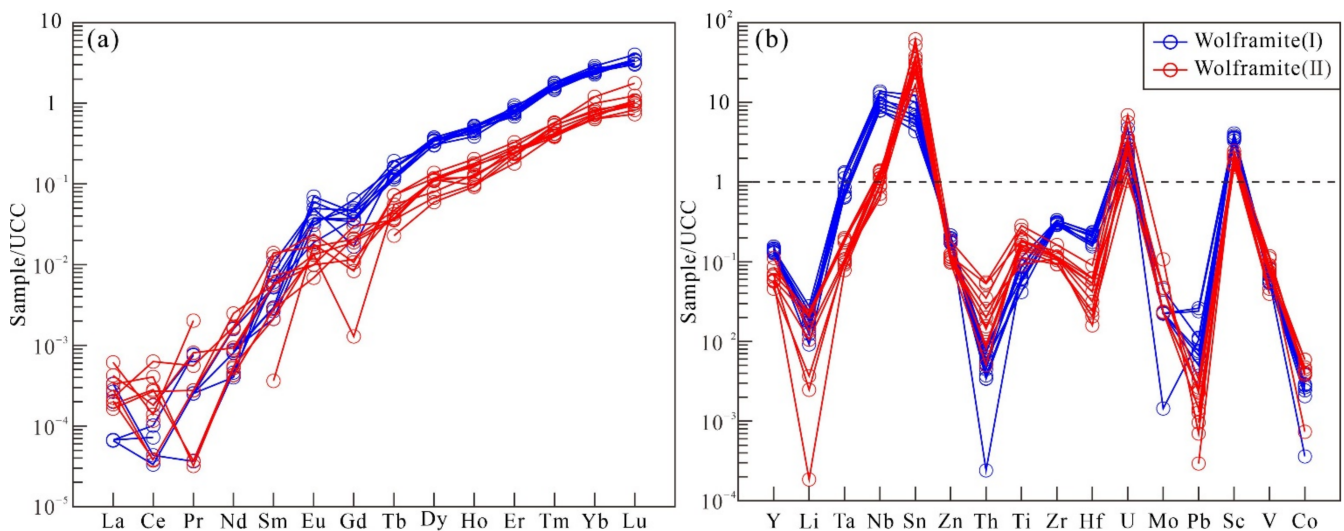


Figure 8. Chemical variations in major and trace elements in wolframite from the two mineralization stages of the Baishitouwa deposit. (a) Mn/(Mn + Fe) versus W diagram; (b) correlation between Mn and Fe contents in wolframite; (c) negative correlation between (W + Nb) and (Fe + Mn) contents.



**Figure 9.** The concentrations of elements in wolframite from two mineralization stages of the Baishitouwa deposit. The bold horizontal line represents the median.

The total REE concentrations of wolframite (I) and wolframite (II) range from 9.75 to 11.95 ppm and 2.59 to 4.83 ppm, respectively. Both wolframite (I) and wolframite (II) are characterized by high heavy REEs (HREEs) concentrations (9.69–11.89 ppm and 2.50–4.70 ppm, respectively), and low light REEs (LREEs) concentrations (0.05–0.11 ppm and 0.03–0.18 ppm, respectively). All REE patterns from wolframite normalized to the upper continental crust (UCC from [91]) show a common preferential enrichment in HREEs relative to LREEs, which are below the detection limit in some samples (Figure 10a). The trace-element patterns normalized to the UCC are used to identify geochemical characteristics of the wolframite crystals [1]. Wolframite grains from both stages show similar trace-element signatures, with relative enrichments in Nb, Sn, U, and Sc, and with relative depletions in Y, Li, Ta, Zn, Th, Ti, Zr, Hf, Mo, Pb, V, and Co (Figure 10b).



**Figure 10.** REE (a) and trace-element (b) patterns of wolframite from the Baishitouwa deposit normalized to the upper continental crust (UCC from [91]).

## 6. Discussion

### 6.1. Timing of W Mineralization

Constraining the timing and duration of mineralization events is critical for understanding ore deposit formation, from both academic and economic viewpoints [39]. At the Baishitouwa deposit, according to the intrusive contact relationship between the granite pluton and the upper Jurassic Zhangjiakou Formation (Figure 3a), Dai [61] considered that the granite pluton formed in the Early Cretaceous. In addition, integrated with geochemical data of the granite pluton and W-related granitoids in South China, Dai [61] concluded that the granite pluton was genetically associated with W mineralization in the Baishitouwa deposit. However, this conclusion contradicts our study.

In our study, a lower intercept  $^{206}\text{Pb}/^{238}\text{U}$  age of  $221.0 \pm 3.4$  Ma ( $1\sigma$ , MSWD = 2.0) (Figure 7) was obtained from in situ U-Pb dating of wolframite from the Baishitouwa deposit, which records a Late Triassic W mineralization event in the district. By collecting the published geochronological data of W-related granitoids and associated W deposits in NE China, Xie et al. [5] determined three episodes of W-related magmatism and mineralization events, namely Triassic (240–250 Ma), Early–Middle Jurassic (170–200 Ma), and Late Jurassic–Early Cretaceous (125–160 Ma). The formation of W mineralization in NE China was initiated in the Early Triassic and peaked in the Late Jurassic–Early Cretaceous [5]. For a long time, researchers have made a comprehensive chronological study of Jurassic and Early Cretaceous granitic magmatism and related W mineralization in this region, whereas the studies of Triassic W mineralization have been in their infancy. Previous geochronologic work only reported two Triassic W deposits, namely the Shazigou W–Mo deposit and Yangjingou W deposit. Peng et al. [31] reported a mean Re–Os age of  $243.8 \pm 1.6$  Ma from five molybdenite samples from the Shazigou W–Mo deposit. Zhao [32] obtained a zircon U–Pb age of  $249.4 \pm 2.7$  Ma and a muscovite  $^{40}\text{Ar}$ – $^{39}\text{Ar}$  age of  $230.8 \pm 1.2$  Ma for the Yangjingou W deposit. It is noteworthy that the Shazigou, Yangjingou, and Baishitouwa deposits are all located along the SXCF, suggesting the formation of these W deposits may be related to the closure of PAO. Xie et al. [5] systematically summarized the tectonic setting of Mesozoic W-mineralized granitoids and associated W deposits, and proposed that Triassic W-mineralized granitoids and associated W deposits formed in a syn- and/or postcollisional setting related to the closure of PAO. According to our wolframite in situ geochronology results, together with previous isotope data, we preliminarily speculate that NE China underwent not only the well-known Jurassic and Early Cretaceous, but also a prevalent Triassic W mineralization event during the Mesozoic period. Consequently, NE China has countless potential for Triassic W mineralization and more attention should be given to the Triassic ore prospecting in the region. The spatial distribution of Triassic W-mineralized granitic intrusions and related W deposits are bound to the closure of PAO, and thus we propose that the Triassic metal exploration should be focused on the two sides of the SXCF.

### 6.2. Factors Controlling Trace-Element Compositions in Wolframite

Wolframite is a typical  $\text{ABO}_4$  compound, with two octahedral sites (A and B) [92]. The wolframite structure is very versatile and occurs with multiple isovalent substitutions [1,42,55,93–98]. The incorporation of other elements in the wolframite structure could significantly change the composition of wolframite, which has been the subject of many studies [1,42,56,58]. In this study, wolframite from different stages at Baishitouwa provides an excellent opportunity to understand the factors controlling trace-element compositions in wolframite.

Several correlations between elements in wolframite are discernible in binary diagrams. It is clearly shown in Figure 11a that Nb and Ta concentrations correlate in the wolframite (I), which indicates that Nb and Ta are incorporated together during wolframite (I) crystallization. In contrast, in wolframite (II), there are no significant positive correlations between Nb and Ta contents (Figure 11a). Furthermore, Nb concentrations in wolframite (I) from this study exhibit positive correlations with Sc, V, Y,  $\Sigma\text{REE}$ , and HREE (Figure 11b–f).

Conformably, these trivalent cations also correlate positively with Ta concentrations in wolframite (I) (Figure 11g–k). In contrast, there are no positive relationships between trivalent cations ( $\text{Sc}^{3+}$ ,  $\text{V}^{3+}$ ,  $\text{Y}^{3+}$ ,  $\Sigma\text{REE}^{3+}$ , and  $\text{HREE}^{3+}$ ) and pentavalent cations ( $\text{Nb}^{5+}$  and  $\text{Ta}^{5+}$ ) in wolframite (II) (Figure 11b–k). All wolframite does not show positive correlations between Nb and LREEs (Figure 11l). The preferential enrichment in HREE (Gd to Lu) compared to LREE (La to Eu) observed in all the wolframite samples is likely constrained by crystallochemical effects. This behavior has been already determined in previous studies on wolframite [1,42,55–59,99]. This preferential incorporation is likely controlled by the ionic radii of the REE. The ionic radii of the HREE ( $\text{Gd}^{3+}$ : 0.94 Å;  $\text{Lu}^{3+}$ : 0.86 Å) are close to those of  $\text{Fe}^{2+}$  (0.78 Å) and  $\text{Mn}^{2+}$  (0.83 Å) in octahedral co-ordination on the A-site [92]. In contrast, the ionic radii of the LREE ( $\text{La}^{3+}$ : 1.03 Å;  $\text{Eu}^{3+}$ : 0.95 Å) are close to those of  $\text{Ca}^{2+}$  (1.0 Å) in octahedral co-ordination of scheelite lattice [92]. It is therefore that the behavior of the REEs in wolframite is opposite to the one in scheelite, and the former tends to incorporate preferentially the HREE [100,101]. The chemical variations described above may be preliminarily explained by the participation of Equation (1), which corresponds to the solid solution  $\text{FeWO}_4\text{-FeNbO}_4$  [93–95].

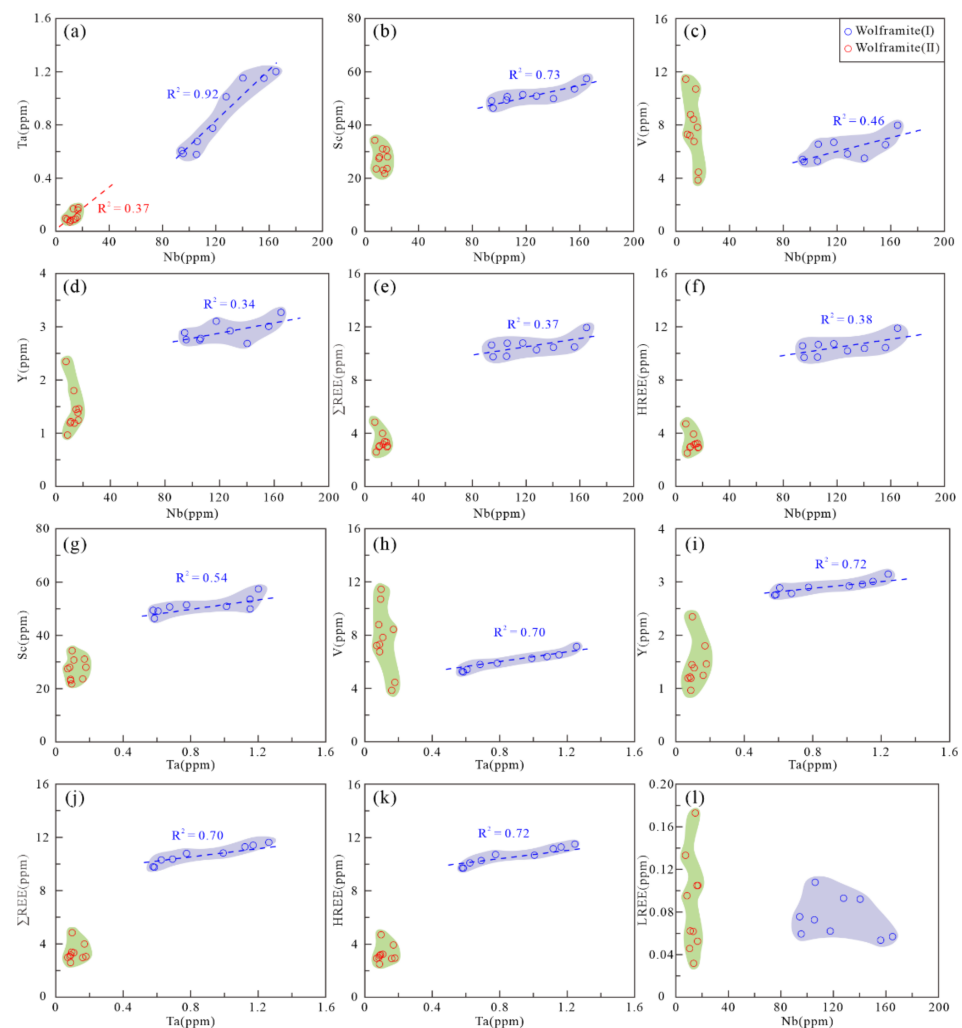
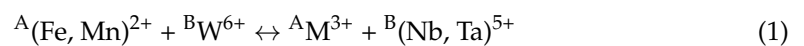
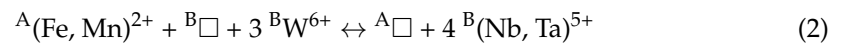


**Figure 11.** (a) Correlation plots of Nb and Ta contents. (b–l) correlation plots of pentavalent and trivalent cations in two generations of wolframite from the Baishitouwa deposit.

Where  $\text{M}^{3+}$  represents the trivalent cations ( $\text{Sc}^{3+}$ ,  $\text{V}^{3+}$ ,  $\text{Y}^{3+}$ ,  $\Sigma\text{REE}^{3+}$ , and  $\text{HREE}^{3+}$ ), and A and B represent the two crystallochemical sites in wolframite ( $\text{ABO}_4$ ; A =  $\text{Fe}^{2+}/\text{Mn}^{2+}$

and  $B = W^{6+}$ ). Another equation (Equation (2)) corresponding to the solid solution  $FeWO_4-FeNb_2O_6$  may also be considered [96]. This reaction supposes the existence of site vacancies ( $\square$ ), which may compensate for each other.



Trace-element compositions suggest that wolframite (I) was controlled by the coupled substitution reactions of Equations (1) and (2). However, neither Equation (1) nor Equation (2) can well explain the composition and variation of trace elements in wolframite (II).

It is clearly shown in Figure 12a–d that Sc contents in wolframite (I) and wolframite (II) show positive correlations with V, Y,  $\Sigma REE$ , and HREE. Furthermore, similar positive correlations are also observed among V, Y,  $\Sigma REE$ , and HREE (Figure 12e–i). This evidence corroborates that these trivalent cations are incorporated together during wolframite crystallization. The Sc contents in wolframite (I) and (II) correlate positively with Ti, Sn, Zr, and Hf contents (Figure 13a–d). Conformably, these tetravalent cations ( $Ti^{4+}$ ,  $Zn^{4+}$ ,  $Zr^{4+}$ ,  $Hf^{4+}$ ) also display a positive relationship with V and Y contents in two generations of wolframite samples (Figure 13e–l). These phenomena suggest that these trivalent and tetravalent cations are incorporated through a similar mechanism during the crystallization of wolframite (I) and (II), as expressed by the coupled substitution reaction of Equation (3) [1,94,97].

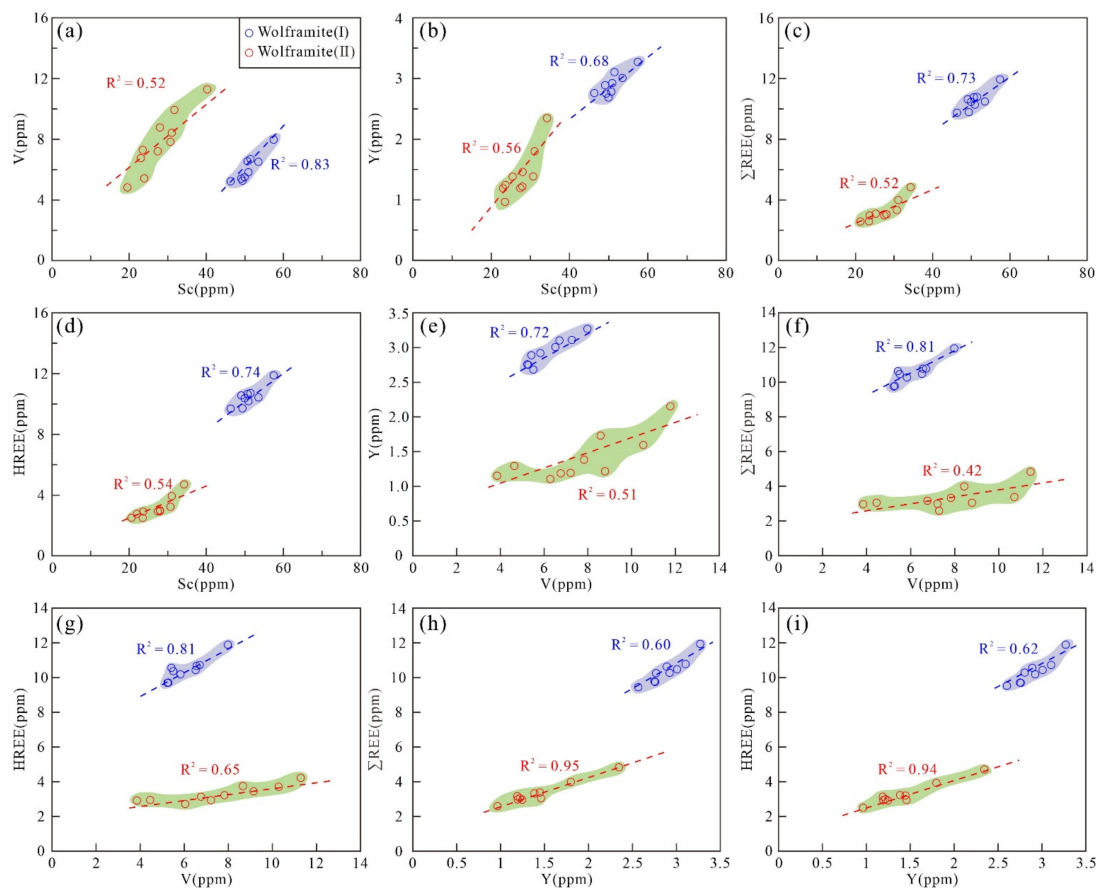
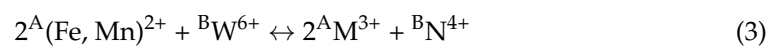


**Figure 12.** Trivalent cations correlation plots for two generations of wolframite from the Baishitouwa deposit. (a) Correlation plots of Sc and V contents; (b) Correlation plots of Sc and Y contents; (c) Correlation plots of Sc and  $\Sigma REE$  contents; (d) Correlation plots of Sc and HREE contents; (e) Correlation plots of V and Y contents; (f) Correlation plots of V and  $\Sigma REE$  contents; (g) Correlation plots of V and HREE contents; (h) Correlation plots of Y and  $\Sigma REE$  contents; (i) Correlation plots of Y and HREE contents.

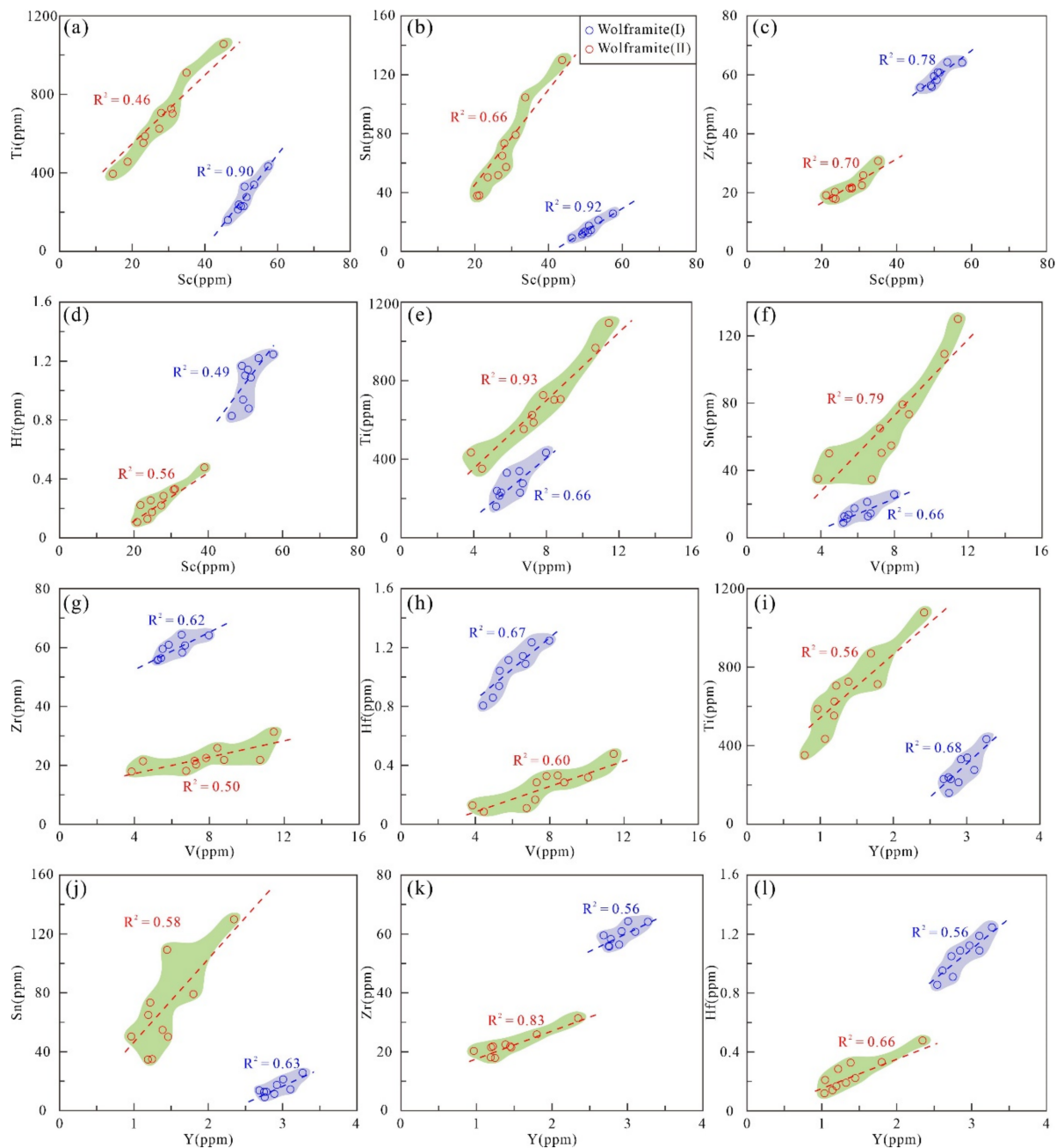


**Figure 13.** Correlation plots of trivalent and tetravalent cations in two generations of wolframite from the Baishitouwa deposit. (a) Correlation plots of Sc and Ti contents; (b) Correlation plots of Sc and Sn contents; (c) Correlation plots of Sc and Zr contents; (d) Correlation plots of Sc and Hf contents; (e) Correlation plots of V and Ti contents; (f) Correlation plots of V and Sn contents; (g) Correlation plots of V and Zr contents; (h) Correlation plots of V and Hf contents; (i) Correlation plots of Y and Ti contents; (j) Correlation plots of Y and Sn contents; (k) Correlation plots of Y and Zr contents; (l) Correlation plots of Y and Hf contents.

$N^{4+}$  represents the tetravalent cations ( $Ti^{4+}$ ,  $Sn^{4+}$ ,  $Zr^{4+}$ ,  $Hf^{4+}$ ). The coupled substitution reaction of Equation (3) played a critical role in controlling the chemical compositions of wolframite from two stages.

Positive correlations between Ti and other tetravalent cations ( $Sn^{4+}$ ,  $Zr^{4+}$ , and  $Hf^{4+}$ ) have been illustrated in Figure 14a–c. Furthermore, the Sn contents also display a positive correlation with Zr and Hf contents in two generations of wolframite (Figure 14d,e). Con-

formably, the positive relationship between Zr and Hf contents is also observed in both wolframite (I) and (II) (Figure 14f). The positive correlation among these tetravalent cations reveals that they are incorporated together into the wolframite lattice, as shown by coupled substitution of Equation (4) [1,94,97].

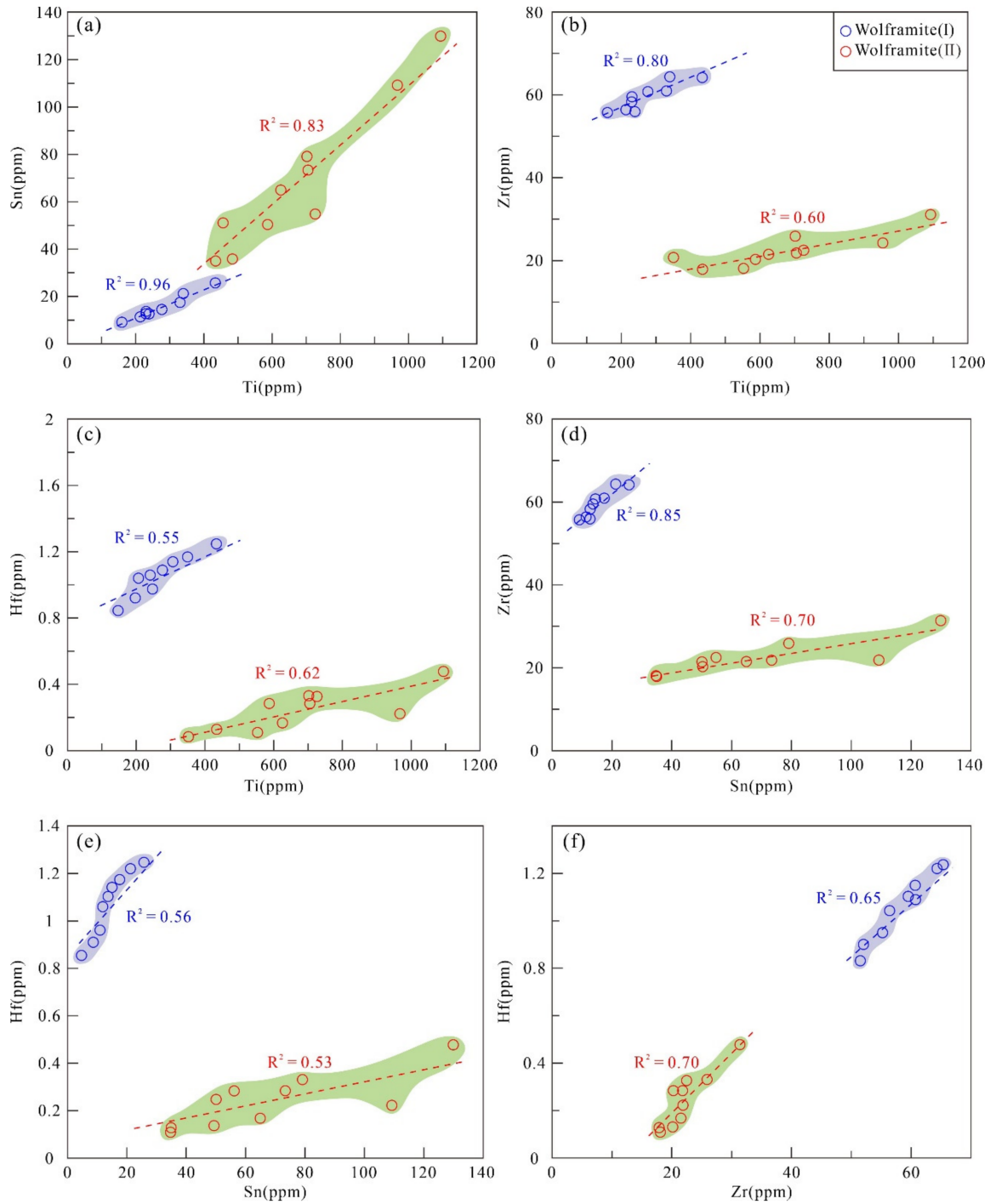


**Figure 14.** Tetravalent cations correlation plots for two generations of wolframite from the Baishi-touwa deposit. (a) Correlation plots of Ti and Sn contents; (b) Correlation plots of Ti and Zr contents; (c) Correlation plots of Ti and Hf contents; (d) Correlation plots of Sn and Zr contents; (e) Correlation plots of Sn and Hf contents; (f) Correlation plots of Zr and Hf contents.

Nb contents in the wolframite (I) show positive correlations with Ti, Sn, Zr, and Hf (Figure 15a–d). Those tetravalent cations also correlate positively with Ta contents in the wolframite (I) (Figure 15e–h). Conformably, it is clearly shown in Figure 15i that (Ti + Sn + Zr + Hf) contents correlate positively with the (Nb + Ta) contents in the wolframite (I). Thus, we infer that these elements are incorporated through a similar mechanism during the crystallization of wolframite (I), as expressed by the coupled substitution reaction of Equation (5) [97,98].

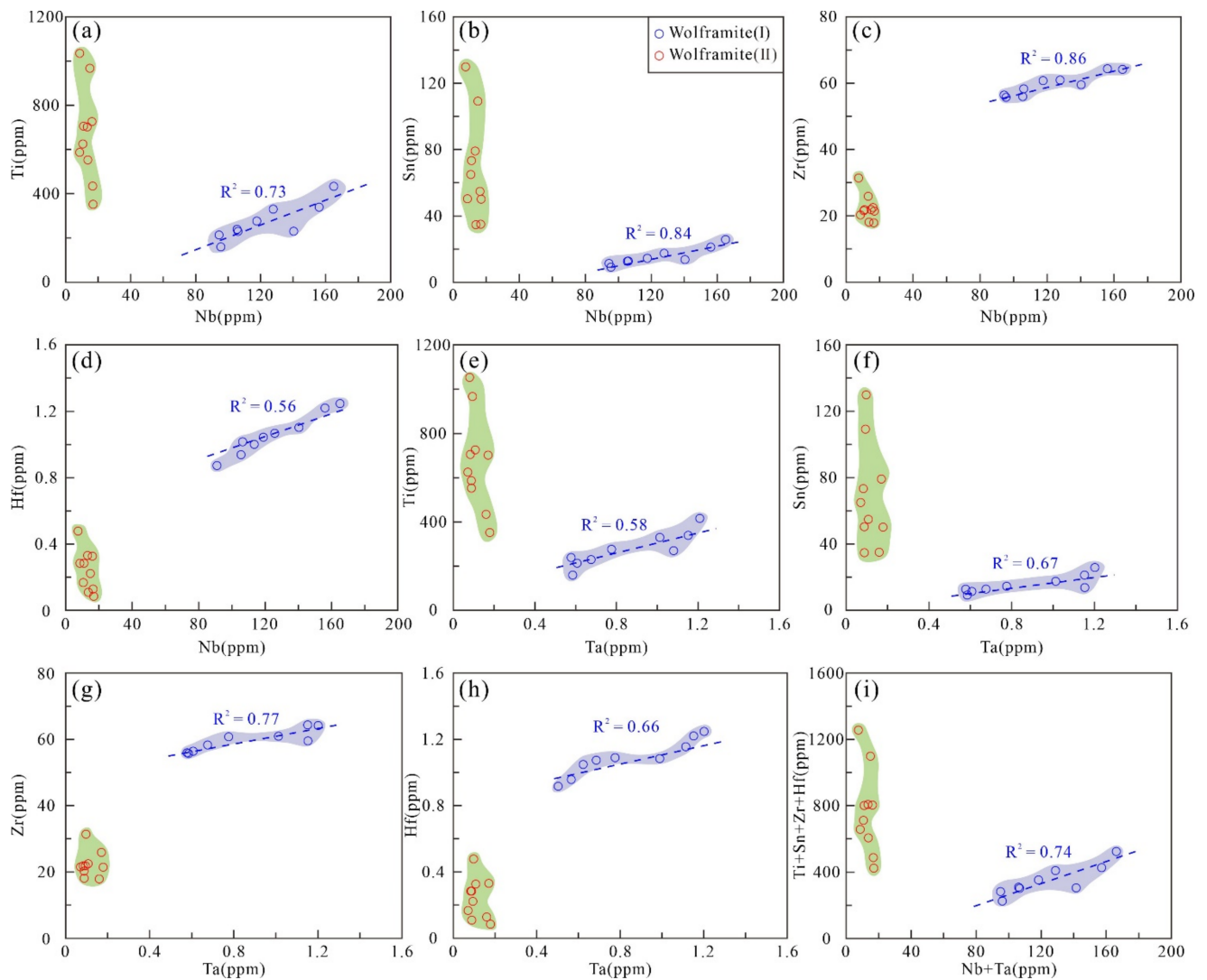
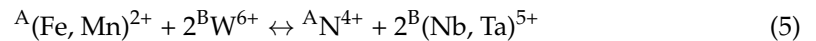


**Figure 15.** Correlation plots of tetravalent and pentavalent cations in two generations of wolframite from the Baishitouwa deposit. (a) Correlation plots of Nb and Ti contents; (b) Correlation plots of Nb and Sn contents; (c) Correlation plots of Nb and Zr contents; (d) Correlation plots of Nb and Hf contents; (e) Correlation plots of Ta and Ti contents; (f) Correlation plots of Ta and Sn contents; (g) Correlation plots of Ta and Zr contents; (h) Correlation plots of Ta and Hf contents; (i) Correlation plots of Nb + Ta and Ti + Sn + Zr + Hf contents.

However, Nb contents in the wolframite (II) do not show positive correlations with Ti, Sn, Zr, and Hf. Those tetravalent cations do not correlate positively with Ta either, indicating that the coupled substitution reaction of Equation (5) cannot explain the trace-element compositions of the wolframite (II).

Based on these findings, it can be concluded that the trace-element compositions of the wolframite (I) and (II) from hydrothermal quartz veins in the Baishitouwa deposit are controlled by crystallochemical parameters (including ionic radius and charge valence). However, the coupled substitution reactions controlling the trace-element compositions of two generations of wolframite are distinct. Five coupled substitution mechanisms can explain the chemical variations in the wolframite (I), whereas the chemical compositions of the wolframite (II) can be elucidated by two coupled substitution mechanisms. Considering that the substitution mechanisms occurred simultaneously during wolframite formation, and thus the substitution mechanisms controlling trace-element compositions of wolframite (I) and wolframite (II) can be unified as shown in Equations (6) and (7), respectively:



The substitution mechanisms controlling trace-element compositions of wolframite in this study are different from those in wolframite from the quartz–wolframite vein-type deposits from the European metallogenic belt and Nanling metallogenic belt [1,42,102], indicating the substitution mechanisms in hydrothermal wolframite from different W deposits are not identical. We preliminarily suggest substitution mechanisms controlling trace-element compositions of wolframite from different stages are different, which should be paid more attention to in future research.

Previous studies revealed that crystallochemical effects and composition of the primary mineralizing fluids are two key controls of wolframite chemistry, with the charge and radius controlled (CHARAC) behavior defined for common igneous rocks, and wolframite by Y/Ho and Zr/Hf ratios [1,58,103]. In the Y/Ho versus Zr/Hf diagram (Figure 16a), almost all two generations of wolframite samples are plotted outside the CHARAC field, indicating that the ionic radius and the charge valence were not the only parameters controlling the mobility of the isovalent trace elements into the fluids precipitating the two generations of wolframite. Hence, the concentrations of elements incorporated during the crystallization of hydrothermal wolframite also reflect the specific chemical composition of the mineralizing fluids [1,58]. Wolframite (I) and (II) from the Baishitouwa deposit distinguish mostly by enrichments in Sc, Ti, Zr, Nb, Sn, and Mg with concentrations ranking from 10 to 10<sup>4</sup> ppm, V, Zn, Y, U, and HREEs with a range of 1 to 10 ppm, and by depletions in Li, Be, B, Cr, Co, Ni, Cu, Pb, Mo, Ag, Cd, Ga, Rb, Sr, Sb, Cs, Ba, Hf, Th, LREEs, etc., in the range of 0.01 to 1 ppm (Figure 9 and Table 3). The high Sc, Ti, Zr, Nb, Sn, and Mg contents in wolframite reveal that these elements are easily incorporated into its crystalline structure, whereas the low contents in other elements (e.g., Cr, Th, Cd, Sr, Pb, Rb, and LREEs) indicate that they are either not incorporated easily into wolframite or present at very low concentrations in the mineralizing fluids owing to low solubility in aqueous solutions. The diagram of ionic radius versus electric charge (Figure 16b) illustrates that the low concentrations of many elements in wolframite can be controlled by crystallochemical parameters (including ionic radius and charge valence). For instance, Rb<sup>+</sup>, Eu<sup>2+</sup>, Sr<sup>2+</sup>, Pb<sup>2+</sup>, Cd<sup>2+</sup>, Bi<sup>3+</sup>, LREE<sup>3+</sup>, and Th<sup>4+</sup> have too large ionic radii (>0.92 Å) making them incompatible to enter the A-site. In contrast, Cr<sup>6+</sup> has a too low ionic radius (<0.56 Å) to enter the B-site into the wolframite structure, whereas it is possible for Cr<sup>3+</sup> (0.61 Å). Symmetrically, charge-compensating elements such as Cu<sup>+</sup>, Li<sup>+</sup>, Zn<sup>2+</sup>, Co<sup>2+</sup>, and Sb<sup>3+</sup> can theoretically enter relatively easily on the A-site, and Ni<sup>3+</sup>, Ga<sup>3+</sup>, Cr<sup>3+</sup>, Co<sup>3+</sup>, and Ge<sup>4+</sup> can theoretically enter relatively easily on the B-site (Figure 16b). However, these elements' contents are significantly low in wolframite from the Baishitouwa deposit, suggesting a control by its concentrations in the mineralizing fluids, and consequently the source of the fluids.

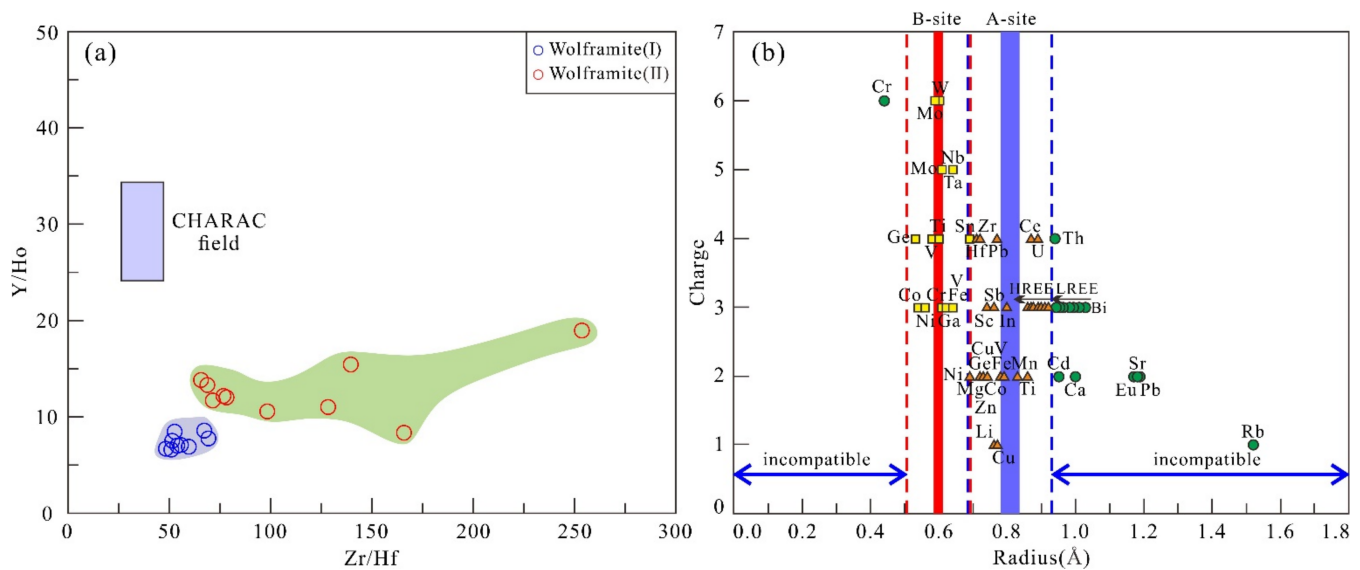


**Figure 16.** (a) Y/Ho versus Zr/Hf ratios in wolframite from the Baishitouwa deposit. The CHARAC field is from [103]. (b) Ionic radius versus electric charge diagram for major and trace elements in octahedral co-ordination in wolframite showing the theoretical occupancy of the A- and B-sites (modified from [1]). Dash lines represent the lower and upper limits of 15% relatively to the lattice site radius corresponding to total substitution (Goldschmidt's rule). Ionic radii data are from [92].

In summary, crystallochemical effects and composition of the primary ore-forming fluids are two key controls of wolframite chemistry in the Baishitouwa deposit, and the substitution mechanisms controlling the trace-element compositions of wolframite from two stage quartz-veins are different.

### 6.3. Source of Ore-Forming Fluids and Materials

Previous studies have demonstrated that trace-elemental (such as Nb, Ta, Sc, and REEs) concentrations in wolframite provide clues to the source of the ore-forming fluids and materials [1,56–58,94,104]. The elements Nb, Ta, and REEs are generally enriched in the high-temperature stage of magmatic crystallization differentiation [105,106]. Subsequently, these elements are incorporated into the tungsten-bearing minerals due to the similarity in the characteristics of electronegativity, ion radius, and ion potential [1,42,57,93,94,97]. Zhang [107] concluded that the concentrations of Nb and Ta in wolframite decline with increasing distance from the parent granite. Gan and Chen [99] performed a comparative element analysis of wolframite in quartz vein-type and greisen-type W deposits and found that they have similar concentrations of  $WO_3$ , MnO, and FeO, but that quartz vein-type deposits have lower Nb, Ta, and Sc concentrations and a higher Nb/Ta ratio compared with greisen-type deposits. Xiong et al. [56] compared the concentrations of Nb, Ta, and Sc in two generations of wolframite and found that stage 1 wolframite has higher concentrations of Nb, Ta, and Sc than stage 2 wolframite. Harlaux et al. [1] proposed that progressive increase in Nb and Ta in wolframite with depth indicated that ore-forming fluids and metals were from hidden granite. Zhang et al. [57] found that Nb and Ta concentrations in wolframite from Piaotang increased from stage 2 to stage 1, and thereby inferred that stage 1 wolframite precipitated from high temperature magma-derived fluids. To decipher the origin of the ore-forming fluids and metals in the Baishitouwa deposit, we collected the published geochemical data of Early Mesozoic W-mineralized granitoids in NE China. It is noteworthy that these W-mineralized granitoids have similar Ta (mainly 0.25–3.06 ppm, average 1.17 ppm) and HREEs (mainly 4.75–28.45, average 15.14) concentrations to the early generation of wolframite (Ta = 0.58–1.20 ppm, HREEs = 9.69–11.89 ppm) in the Baishitouwa. In contrast, these W-mineralized granitoids have lower Nb concentrations (2.76–30.70 ppm) than early generation wolframite (Nb = 94.35–165 ppm) in the

Baishitouwa, which could explain the tendency for Nb incorporation in wolframite lattice during magmatic–hydrothermal evolution [1,105,106]. Ballouard et al. [108] pointed out that Nb is slightly more mobile than Ta, suggesting that magmatic–hydrothermal processes account for the decrease in the Nb/Ta ratio in peraluminous granites that may be related to Ta, Cs, Nb, Be, Sn, and W mineralization. Xie et al. [5] concluded that Mesozoic W-mineralized granitoids in NE China have lower Nb/Ta ratios than contemporary W-barren granitoids. According to Zhang [109], the concentration of Sc can reach 10–1000 ppm in granitic magma and its residual solution during the period of late crystallization, which suggests that the ore-forming fluid may have originated from deep magma. The Sc concentrations of wolframite (I) and wolframite (II) range from 46.32–57.43 ppm and 21.78–34.24 ppm, respectively, which suggest that the ore-forming fluids of the Baishitouwa deposit were derived from granitic magma. In the LREE–Middle REE (MREE)–HREE diagram [110], wolframite from quartz–wolframite vein-type deposits in South China and French Massif Central all plot near the corner of HREE (Figure 17), and the ore-forming fluids and materials of these deposits have been corroborated to originate from coeval granitoids [1,56–59]. The characteristics of the LREE–MREE–HREE in wolframite from the Baishitouwa deposit are similar to those of granitic intrusion-related quartz–wolframite vein-type deposits worldwide, thereby suggesting that the initial ore-forming fluids and materials were of magmatic origin (Figure 17).

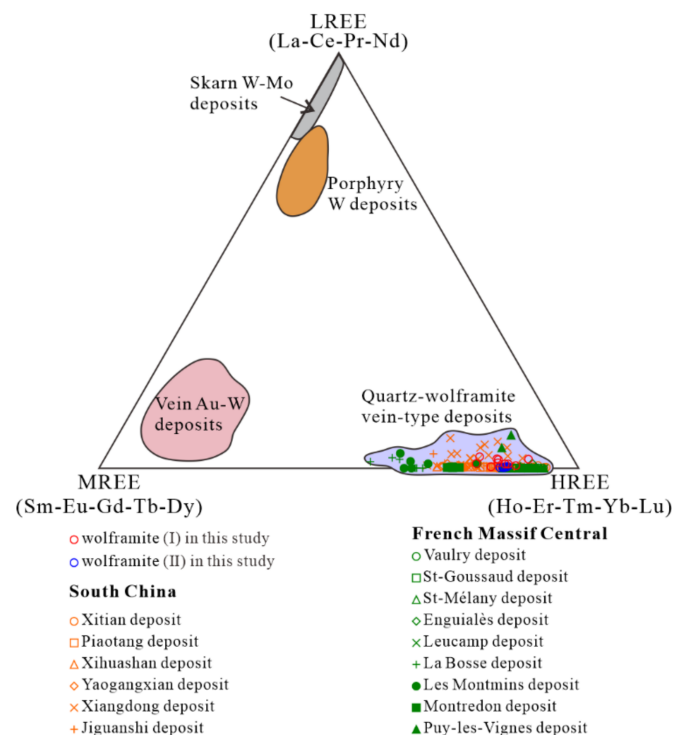


**Figure 17.** A LREE–MREE–HREE diagram showing the composition of different types of W deposits in the world (modified after [110]). The data of wolframite from quartz–wolframite vein-type deposits are listed in Supplementary Material Table S1.

Due to the similar ionic radii and valences of ‘geochemical twin’ elements, these elemental ratios (e.g., Nb/Ta and Y/Ho) tend to remain fairly stable in a given magmatic–hydrothermal system, allowing their use as a fluid source indicator [103,108,111,112]. If ore-forming fluids originated from magmas only, the wolframite crystallized from such fluids should exhibit a narrow range of Y/Ho ratios [103,111]. Zhang et al. [113] argued that the relatively high Nb (more than 4.0 ppm), Ta (more than 0.01 ppm) and consistent Nb/Ta ratios in scheelite from the Xuefeng Uplift Belt are indicative of a magmatic source. Cao et al. [112] considered that the relatively invariant Y/Ho ratios in both generations of scheelite from the Helukou deposit indicate that they were precipitated from a single

source fluid. Cao et al. [112] also noted that Y/Ho ratios of scheelite from the Helukou deposit are consistent with previously published Y/Ho ratios for the Middle Jurassic Guposhan granites, thereby indicating a genetic link between W mineralization and Middle Jurassic Guposhan granites. In the present study, wolframite (I) and (II) from the Baishitouwa deposit have consistent Nb/Ta ratios of 121.76–182.58 and 76.91–158.27, respectively. Figure 18 shows that most wolframite from the South China and French Massif Central display a relatively narrow range of Y/Ho ratios (5–35). The wolframite from the Baishitouwa deposit also shows a narrow range of Y/Ho ratios (6.62–18.97), which is similar to the Y/Ho ratios of granitic intrusion-related quartz–wolframite vein-type deposits worldwide (5–35) and the Mesozoic highly fractionated W-mineralized granitoids (5.07–27.97), implying that the W mineralization in the Baishitouwa deposit is genetically related to an underlying highly fractionated granite.

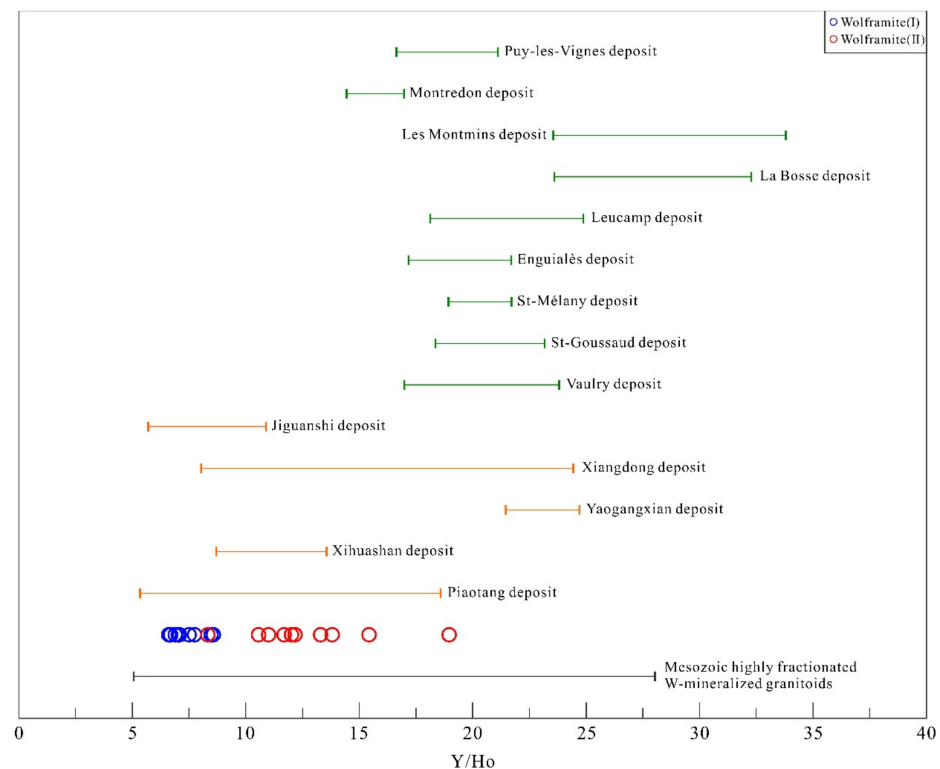


**Figure 18.** Y/Ho ratios for wolframite and W-mineralized granitoids. Data of wolframite from the Piaotang, Xihuashan, Yaogangxian, Xiangdong, and Jiguanshi deposits in South China are listed in Table S1. Data of wolframite from the Vaulry, St-Goussaud, St-Mélany, Enguialès, Leucamp, La Bosse, Les Montmins, Montredon-Labessonnié, and Puy-les-Vignes deposits in French Massif Central are listed in Table S1. Data of Early Mesozoic W-mineralized granitoids in NE China are listed in Supplementary Material Table S2.

Generally, W mineralization is associated with highly fractionated granites, as corroborated by amounts of cases worldwide [3,5,6,114–123]. As previously mentioned, the granite pluton exposed in the eastern part of the district intruded into the Upper Jurassic Zhangjiakou Formation, indicating they may form during the Early Cretaceous [61], whereas a lower intercept  $^{206}\text{Pb}/^{238}\text{U}$  age of  $221.0 \pm 3.4$  Ma ( $1\sigma$ , MSWD = 2.0) (Figure 7) obtained from in situ U-Pb dating of wolframite from the Baishitouwa deposit records a Late Triassic W mineralization event in this district. The inconsistent age data indicate that there is no genetic relationship between granite and W mineralization, and the granite records a late postmineralization magmatic event. A huge number of studies have demonstrated that concealed granite is widely distributed in quartz–wolframite vein-type deposits, which provides the source of heat and materials for W mineralization [1,6,40,58,120,124–126]. These W

deposits generally do not display granitic intrusion on the surface, or even within the depth controlled by drilling. The ore-forming concealed granite plutons are considered to have better preservation conditions for hydrothermal W deposits than their exposed counterparts, since the deposits are not affected by remarkable surficial weathering or erosion [124].

In summary, we preliminarily conclude that the ore-forming fluids and materials of the Baishitouwa deposit were derived from an underlying highly fractionated granite.

#### 6.4. Fluid Evolution Indicated by Compositions of Wolframite

Variations of trace-element compositions in wolframite have been used to decipher the evolutionary history and physicochemical conditions of the ore-forming fluids in many studies [56–58,127]. Brugger et al. [127] proposed that the precipitation of tungsten minerals could effectively alter the compositions of fluids. Zhang et al. [57] found that the early wolframite would lower REE, Nb, and Ta in the mineralizing fluids, leading to depletion of these elements in the later ones. Zhang et al. [57] also noted that although both the two generations of wolframite from the Xihuashan and Piaotang deposit have different REE contents and Eu anomalies, they display similar left-dipped REE<sub>N</sub> patterns, implying that compositional variation of fluids is likely driven by crystallization of wolframite during the processes of fluid evolution. In this study, wolframite (I) contains higher Nb (94.35–165 ppm), Ta (0.58–1.20 ppm), and REEs (9.75–11.95 ppm) concentrations than wolframite (II) (Nb = 7.46–16.86 ppm, Ta = 0.07–0.18 ppm, and REEs = 2.59–4.83 ppm) (Figure 9), and they are characterized by similar left-dipped REE<sub>N</sub> and trace-element patterns (Figure 10). We infer that the crystallization of the early generation of wolframite with high Nb, Ta, and REE would lower these elements in the mineralizing fluids. Therefore, a late generation of wolframite precipitating from evolved fluids would contain relatively lower concentrations of these elements.

Nb, Ta, and Sc concentrations in wolframite may be associated with Fe and Mn concentrations and the crystallization temperature, whereas the pH, Eh, and composition of the ore-forming fluid are dependent on the Nb, Ta, and Sc concentrations [128]. Specifically, a low pH and high Eh provide favorable conditions for the enrichment of Nb and Ta in wolframite, whereas a low-pH and low-Eh ore-forming fluid containing F<sup>-</sup> and/or PO<sub>4</sub><sup>3-</sup> complexes provides ideal conditions for the enrichment of Sc [56,58,128]. The LA-ICP-MS analysis of wolframite from the Baishitouwa deposit shows that wolframite (I) contains more Nb, Ta, and Sc than does wolframite (II), which suggests that the stage 1 fluid has low pH and high Eh, offering favorable conditions for the enrichment of Nb and Ta. For Sc, we infer that the ore-forming fluid might have originated from or flowed through material abundant in Sc, giving the fluid a high initial Sc concentration, resulting in the abundance of Sc in wolframite (I) despite the high Eh environment.

Eu is a redox-sensitive element and has two ionic valences: Eu<sup>3+</sup> and Eu<sup>2+</sup> [92]. Compared with Eu<sup>2+</sup> (1.17 Å), the ionic radius of Eu<sup>3+</sup> (0.95 Å) is much closer to those of Fe<sup>2+</sup> (0.78 Å) and Mn<sup>2+</sup> (0.83 Å) [92] so that the partition coefficient of Eu<sup>3+</sup> between wolframite and fluids is much higher than that of Eu<sup>2+</sup>. In this study, wolframite (I) has higher Eu concentrations than wolframite (II) (Figure 19a). This finding implies that Eu in the stage 1 fluid occurs mainly as Eu<sup>3+</sup> in a relatively oxidized environment, whereas Eu<sup>2+</sup> was primarily concentrated in the relatively reduced stage 2 fluids. Cr can enter the wolframite lattice as Cr<sup>3+</sup> (0.61 Å), whereas Cr<sup>6+</sup> has a too low ionic radius (<0.56 Å) to enter the B-site into the wolframite structure [1,92]. Therefore, wolframite precipitated from oxidizing fluids tends to contain low Cr concentrations. In addition, Pb concentrations in wolframite can also be a tracer of the redox conditions of the mineralizing fluids. Under oxidizing conditions, Pb<sup>4+</sup> readily enters the wolframite lattice by the substitution mechanism of Equation (5), leading to Pb enrichment [1,92]. In contrast, under reducing conditions, Pb<sup>2+</sup> combines with S<sup>2-</sup> to form galena. Hence, the redox conditions must be changed during the process of galena precipitation. The variation of oxygen fugacity does not affect the precipitation of wolframite, but galena tends to precipitate under a relatively reducing environment. Therefore, the variation of lead content in wolframite shows changes in

physical and chemical conditions of ore-forming fluids in Baishitouwa. In this study, wolframite (I) has higher Cr (0.44–20.12 ppm) and lower Pb (0.01–0.06 ppm) concentrations than wolframite (II) (Cr = 0.10–0.42 ppm, Pb = 0.06–0.45 ppm) (Figure 19b,c). Mineralogical evidence suggests that Pb mainly occurs as galena during the quartz–polymetallic sulfides stage, and that galena had not precipitated during stages 1 and 2. This phenomenon indicates that the ore-forming fluid changed from the oxidation state to the relative reduction state during the evolution from stage 1 to 2, increasing the proportion of  $Pb^{2+}$  in the ore-forming fluids. These  $Pb^{2+}$  ions eventually precipitated as galena in the quartz–polymetallic sulfides stage. Furthermore, the mineral assemblages can also provide evidence for the change in the metallogenic environment. Stage 1 is the main W mineralization stage and characterized by abundant tabular crystals of wolframite, whereas sulfides are absent in this stage (Figure 4a,b). In contrast, stage 2 is featured with an assemblage of wolframite, pyrite, and chalcopyrite (Figure 4d). The distinct mineral assemblages in stages 1 and 2 implies different redox conditions.

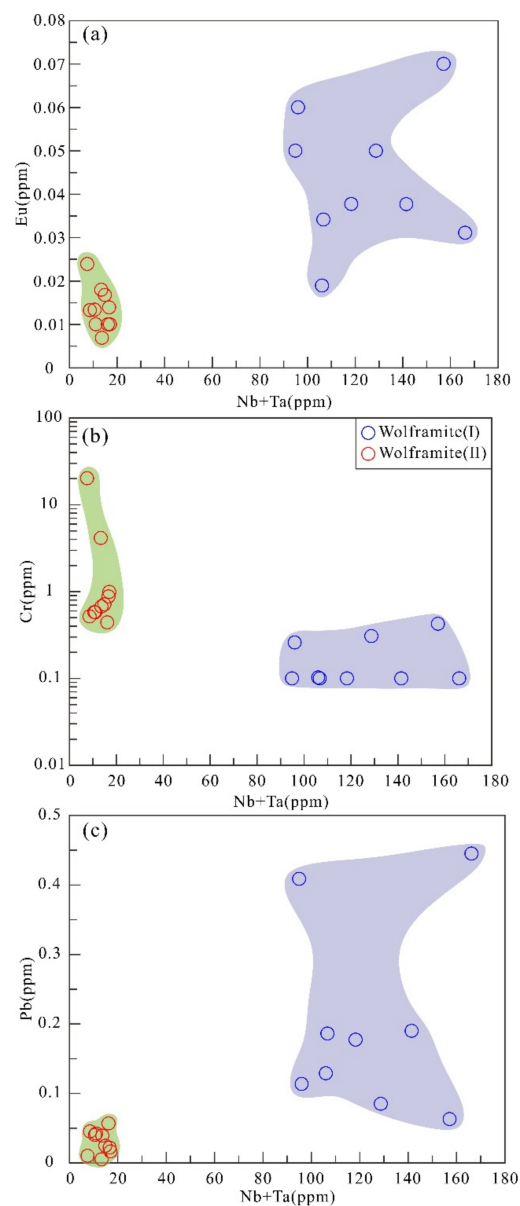


**Figure 19.** (a) Plot of Eu versus (Nb + Ta) of wolframite. (b) Plot of Cr versus (Nb + Ta) of wolframite. (c) Plot of Pb versus (Nb + Ta) of wolframite.

In summary, the ore-forming fluids in Baishitouwa changed from an oxidized to a relatively reduced state during the evolution from stage 1 to stage 2.

## 7. Conclusions

(1) In situ U-Pb dating of wolframite from the Baishitouwa deposit by LA-SF-ICP-MS yielded a lower intercept  $^{206}\text{Pb}/^{238}\text{U}$  age of  $221.0 \pm 3.4$  Ma, which records a late Triassic W mineralization event in the Baishitouwa deposit.

(2) Two generations of wolframite are identified, which have distinctly major- and trace-element characteristics. Wolframite (I) contains higher Nb, Ta, Sc, Zr, Hf, Pb, and Eu concentrations, lower Ti, Sn, Cr, and Th concentrations, and lower Mn/(Mn + Fe) ratios than wolframite (II). Both wolframite (I) and (II) have similar trace elements and LREE-depleted patterns.

(3) Crystallochemical effects and the composition of primary ore-forming fluids are two key controls of wolframite chemistry in the Baishitouwa deposit. The substitution mechanisms controlling the compositions of two generations of wolframite are distinct. Trace-element compositions suggest that wolframite (I) was controlled by the substitution mechanism of  $4^{\text{A}}(\text{Fe}, \text{Mn})^{2+} + 8^{\text{B}}\text{W}^{6+} + \text{B}\square \leftrightarrow 3^{\text{A}}\text{M}^{3+} + \text{A}\text{N}^{4+} + 7^{\text{B}}(\text{Nb}, \text{Ta})^{5+} + 2^{\text{B}}\text{N}^{4+}$ , whereas wolframite (II) was controlled by the substitution mechanism of  $^{\text{A}}(\text{Fe}, \text{Mn})^{2+} + \text{A}\square + 2^{\text{B}}\text{W}^{6+} \leftrightarrow 2^{\text{A}}\text{M}^{3+} + 2^{\text{B}}\text{N}^{4+}$ .

(4) In situ LA-ICP-MS trace-element compositions of wolframite indicate that the ore-forming fluids and materials of the Baishitouwa deposit were mainly derived from an underlying highly fractionated granite.

(5) According to the mineralogical observation and various Nb, Ta, Sc, Eu, Cr, and Pb contents in the two generations of wolframite, we proposed that the ore-forming fluids of the Baishitouwa deposit changed from an oxidized to a relatively reduced state during the evolution from stage 1 to stage 2.

**Supplementary Materials:** The following supporting information can be downloaded at: <https://www.mdpi.com/article/10.3390/min12050515/s1>, Table S1: Chemical composition of wolframite in quartz–wolframite vein-type deposits from South China and French Massif Central; Table S2: Major and trace-element compositions of Mesozoic W-mineralized granitoids in the Xing–Meng Orogenic Belt.

**Author Contributions:** Conceptualization, W.X. and Q.Z.; methodology, T.L.; formal analysis, W.X.; investigation, W.X., Q.Z., R.W., and J.W.; writing—original draft preparation, W.X.; writing—review and editing, Q.Z. and L.Z.; visualization, W.X.; supervision, Q.Z.; funding acquisition, Q.Z. All authors have read and agreed to the published version of the manuscript.

**Funding:** This research was funded by the National Natural Science Foundation of China, grant number 91962104.

**Acknowledgments:** We are grateful to three anonymous reviewers for their constructive comments which greatly help in improving our paper. We would like to thank Yun-Ze Huang and Hong-Fang Chen from the Wuhan Sample Solution Analytical Technology Co., Ltd. for their help during the EPMA and LA-ICP-MS analysis of wolframite. We also thank Yan-Wen Tang and Jun-Jie Han from the State Key Laboratory of Ore Deposit Geochemistry, Institute of Geochemistry, Chinese Academy of Sciences for help with in situ wolframite LA-SF-ICP-MS analysis.

**Conflicts of Interest:** The authors declare no conflict of interest.

## References

1. Harlaux, M.; Mercadier, J.; Marignac, C.; Peiffert, C.; Cloquet, C.; Cuney, M. Tracing metal sources in peribatholithic hydrothermal W deposits based on the chemical composition of wolframite: The example of the Variscan French Massif Central. *Chem. Geol.* **2018**, *479*, 58–85. [[CrossRef](#)]
2. Romer, R.L.; Kroner, U. Phanerozoic tin and tungsten mineralization—Tectonic controls on the distribution of enriched protoliths and heat sources for crustal melting. *Gondwana Res.* **2016**, *31*, 60–95. [[CrossRef](#)]
3. Cao, J.Y.; Yang, X.Y.; Du, J.G.; Wu, Q.H.; Kong, H.; Li, H.; Wan, Q.; Xi, X.S.; Gong, Y.S.; Zhao, H.R. Formation and geodynamic implication of the Early Yanshanian granites associated with W–Sn mineralization in the Nanling range, South China: An overview. *Int. Geol. Rev.* **2018**, *60*, 1744–1771. [[CrossRef](#)]

4. Wang, R.L.; Zeng, Q.D.; Zhang, Z.C.; Zhou, L.L.; Qin, K.Z. Extensive mineralization in the eastern segment of the Xingmeng orogenic belt, NE China: A regional view. *Ore Geol. Rev.* **2021**, *135*, 104204. [[CrossRef](#)]
5. Xie, W.; Zeng, Q.D.; Wang, R.L.; Wu, J.J.; Zhang, Z.M.; Li, F.C.; Zhang, Z. Spatial-temporal distribution and tectonic setting of Mesozoic W-mineralized granitoids in the Xing-Meng Orogenic Belt, NE China. *Int. Geol. Rev.* **2021**, 1–40. [[CrossRef](#)]
6. Zhao, Z.; Fu, T.Y.; Gan, J.W.; Liu, C.; Wang, D.H.; Sheng, J.F.; Li, W.B.; Wang, P.A.; Yu, Z.F.; Chen, Y.C. A synthesis of mineralization style and regional distribution and a proposed new metallogenic model of Mesozoic W-dominated polymetallic deposits in South China. *Ore Geol. Rev.* **2021**, *133*, 104008. [[CrossRef](#)]
7. Werner, A.B.T.; Sinclair, W.D.; Amey, E.B. International Strategic Mineral Issues Summary Report-Tungsten (Ver. 1.1, November 2014). In *U.S. Geological Survey Circular 930-O*; U.S. Geological Survey: Reston, VA, USA, 2014; pp. 1–74.
8. Zeng, Q.D.; Liu, J.M.; Chu, S.X.; Wang, Y.B.; Sun, Y.; Duan, X.X.; Zhou, L.L. Mesozoic molybdenum deposits in the East Xingmeng orogenic belt, northeast China: Characteristics and tectonic setting. *Int. Geol. Rev.* **2012**, *54*, 1843–1869. [[CrossRef](#)]
9. Zeng, Q.D.; Qin, K.Z.; Liu, J.M.; Li, G.M.; Zhai, M.G.; Chu, S.X.; Guo, Y.P. Porphyry molybdenum deposits in the Tianshan–Xingmeng orogenic belt, northern China. *Int. J. Earth Sci.* **2015**, *104*, 991–1023. [[CrossRef](#)]
10. Ouyang, H.G.; Mao, J.W.; Zhou, Z.H.; Su, H.M. Late Mesozoic metallogeny and intracontinental magmatism, southern Great Xing’an Range, northeastern China. *Gondwana Res.* **2015**, *27*, 1153–1172. [[CrossRef](#)]
11. Ouyang, H.G.; Mao, J.W.; Santosh, M.; Zhou, J.; Zhou, Z.H.; Wu, Y.; Hou, L. Geodynamic setting of Mesozoic magmatism in NE China and surrounding regions: Perspectives from spatio-temporal distribution patterns of ore deposits. *J. Asian Earth Sci.* **2013**, *78*, 222–236. [[CrossRef](#)]
12. Xie, W.; Wen, S.Q.; Zhang, G.L.; Tang, T.Q. Geochronology, fluid inclusions, and isotopic characteristics of the Dongjun Pb–Zn–Ag deposit, Inner Mongolia, NE China. *Acta Geol. Sin.* **2021**, *95*, 1611–1633. [[CrossRef](#)]
13. Li, J.J.; Zhou, Y.; Dang, Z.C.; Zhao, Z.L.; Li, C.; Qu, W.J.; Cao, Z.C.; Yang, G.J.; Fu, C.; Tang, W.L. Re–Os isotopic dating of molybdenites from the Sansheng W–Mo deposit in Huada County, Inner Mongolia, and its geological significance. *Geol. Bull. China* **2016**, *35*, 531–536.
14. Zeng, Q.D.; Sun, Y.; Chu, S.X.; Duan, X.X.; Liu, J.M. Geochemistry and geochronology of the Dongshanwan porphyry Mo–W deposit, Northeast China: Implications for the Late Jurassic tectonic setting. *J. Asian Earth Sci.* **2015**, *97*, 472–485. [[CrossRef](#)]
15. Xiang, A.P.; Chen, Y.C.; Bagas, L.; She, H.Q.; Kang, Y.J.; Yang, W.S.; Li, C.J. Molybdenite Re–Os and U–Pb zircon dating and genesis of the Dayana W–Mo deposit in eastern Ujumchin, Inner Mongolia. *Ore Geol. Rev.* **2016**, *78*, 268–280. [[CrossRef](#)]
16. Xiang, A.P.; Chen, Y.C.; She, H.Q.; Li, G.M.; Li, Y.X. Chronology and geochemical characteristics of granite in Weilianhe of Inner Mongolia and its geological significance. *Geol. China* **2018**, *45*, 963–976.
17. Xiang, A.P.; She, H.Q.; Chen, Y.C.; Qin, D.J.; Wang, Y.J.; Han, Z.G.; Kang, Y.J. Ar–Ar age of muscovite from the greisenization alteration zones of the Honghuaerji tungsten polymetallic deposit, Inner Mongolia, and its geological significance. *Rock Miner. Anal.* **2016**, *35*, 108–116.
18. Hao, Y.J.; Ren, Y.S.; Zhao, H.L.; Zou, X.T.; Chen, C.; Hou, Z.S.; Qu, W.J. Re–Os isotopic dating of the molybdenite from the Cuihongshan W–Mo polymetallic deposit in Heilongjiang Province and its geological significance. *J. Jilin Univ.* **2013**, *43*, 1840–1850.
19. Shao, J.; Li, X.R.; Yang, H.Z. Zircon SHRIMP U–Pb dating of granite in the Cuihongshan polymetallic deposit and its geological implications. *Acta Geosci. Sin.* **2011**, *32*, 163–170.
20. Yang, F.; Sun, J.G.; Wang, Y.; Fu, J.Y.; Na, F.C.; Fan, Z.Y.; Hu, Z.Z. Geology, Geochronology and Geochemistry of Weilasituo Sn–Polymetallic Deposit in Inner Mongolia, China. *Minerals* **2019**, *9*, 104. [[CrossRef](#)]
21. Gao, X.; Zhou, Z.; Breiter, K.; Ouyang, H.; Liu, J. Ore-formation mechanism of the Weilasituo tin–polymetallic deposit, NE China: Constraints from bulk-rock and mica chemistry, He–Ar isotopes, and Re–Os dating. *Ore Geol. Rev.* **2019**, *109*, 163–183. [[CrossRef](#)]
22. Li, J.J.; Fu, C.; Tang, W.L.; Li, H.M.; Lin, Y.X.; Zhang, T.; Wang, S.G.; Zhao, Z.L.; Dang, Z.C.; Zhao, L.J. The metallogenic age of the Shamai wolframite deposit in Dong Ujimqin Banner, Inner Mongolia. *Geol. Bull. China* **2016**, *35*, 524–530.
23. Wang, Y.H.; Zhang, F.F.; Liu, J.J.; Xue, C.J.; Zhang, Z.C. Genesis of the Wurinitu W–Mo deposit, Inner Mongolia, northeast China: Constraints from geology, fluid inclusions and isotope systematics. *Ore Geol. Rev.* **2018**, *94*, 367–382. [[CrossRef](#)]
24. Yang, Z.H.; Wang, J.P.; Liu, J.J.; Wang, S.G.; Wang, Q.Y.; Kang, S.G. Characteristics and its geological significance of fluid inclusions of the Wurinitu W–Mo deposit in Inner Mongolia, China. *Earth Sci.–J. China Univ. Geosci.* **2012**, *37*, 1268–1278.
25. Wang, R.L.; Zeng, Q.D.; Zhang, Z.C.; Guo, Y.P.; Lu, J.H. Fluid Evolution, H–O Isotope and Re–Os Age of Molybdenite from the Baiyinhan Tungsten Deposit in the Eastern Central Asian Orogenic Belt, NE China, and Its Geological Significance. *Minerals* **2020**, *10*, 664. [[CrossRef](#)]
26. Yang, Z.H.; Wang, J.P.; Liu, J.J.; Wang, S.G.; Wang, Q.Y.; Kang, S.G.; Zhang, J.X.; Zhao, Y. Isotope geochemistry of the Wurinitu W–Mo deposit in Sunid Zuoqi, Inner Mongolia, China. *Geoscience* **2013**, *27*, 13–23.
27. Guo, Z.J.; Li, J.W.; Xu, X.Y.; Song, Z.Y.; Dong, X.Z.; Tian, J.; Yang, Y.C.; She, H.Q.; Xiang, A.P.; Kang, Y.J. Sm–Nd dating and REE Composition of scheelite for the Honghuaerji scheelite deposit, Inner Mongolia, Northeast China. *Lithos* **2016**, *261*, 307–321. [[CrossRef](#)]
28. Chen, X.; Liu, J.J.; Zhang, D.H.; Zhang, Q.B.; Yang, S.S.; Li, Y.C.; Cao, Q. Re–Os dating of molybdenites and S–Pb isotopic characteristics of the Cuihongshan iron polymetallic deposit, Heilongjiang Province. *Acta Petrol. Sin.* **2017**, *33*, 529–544.
29. Shang, Q.Q.; Ren, Y.S.; Chen, C.; Zhao, H.L.; Li, C.H. Metallogenic age and ore-forming material source of Yangjin’gou gold deposit in eastern Yanbian region. *Gold* **2017**, *38*, 7–12.

30. Xie, W.; Zeng, Q.D.; Yang, J.H.; Li, R.; Zhang, Z.; Wang, R.L.; Wu, J.J. Petrogenesis, W metallogenic and tectonic implications of granitic intrusions in the southern Great Xing'an Rang W belt, NE China: Insights from the Narenwula Complex. *Geol. Mag.* **2022**, *159*, 593–627. [[CrossRef](#)]
31. Peng, N.L.; Xi, X.S.; Kong, H.; Chen, Z.F.; Wang, G. Re-Os isotopic dating of molybdenites from the Shazigou W-Mo polymetallic deposit, Inner Mongolia and its geological implications. *Geol. Explor.* **2015**, *51*, 838–848.
32. Zhao, H.L. Ore Genesis and Geodynamic Settings of Tungsten Deposits in Eastern Jilin and Heilongjiang Provinces. Ph.D. Thesis, Jilin University, Changchun, China, 2014.
33. Cui, Y.X. Geological characteristics and genesis of Narenwula copper polymetallic deposit. *Basic Sci.* **2013**, *5*, 103–104.
34. Zhang, Z.C. Geological characteristics, ore controlling factors and prospecting direction of W-Bi-Ag polymetallic ore deposit in Narenwula mining area, Xianghuang Banner, Inner Mongolia. *World Nonferrous Met.* **2020**, *1*, 94–95.
35. Liu, C.; Deng, J.F.; Kong, W.Q.; Xu, L.Q.; Zhao, G.C.; Luo, Z.H.; Li, N. LA-ICP-MS zircon U-Pb geochronology of the fine-grained granite and molybdenite Re-Os dating in the Wurinitu molybdenum deposit, Inner Mongolia, China. *Acta Geol. Sin.* **2011**, *85*, 1057–1066. [[CrossRef](#)]
36. Hu, P.; Nie, F.J.; He, Y.; Zhang, Y.; Liu, Y. Geological features and fluid inclusions of Shamai tungsten deposit, Inner Mongolia. *Miner. Depos.* **2005**, *24*, 603–612.
37. Liu, Y.J.; Li, W.M.; Feng, Z.Q.; Wen, Q.B.; Neubauer, F.; Liang, C.Y. A review of the Paleozoic tectonics in the eastern part of Central Asian Orogenic Belt. *Gondwana Res.* **2017**, *43*, 123–148. [[CrossRef](#)]
38. Wu, F.Y.; Sun, D.Y.; Ge, W.C.; Zhang, Y.B.; Grant, M.L.; Wilde, S.A.; Jahn, B.M. Geochronology of the Phanerozoic granitoids in northeastern China. *J. Asian Earth Sci.* **2011**, *41*, 1–30. [[CrossRef](#)]
39. Stein, H.J. Dating and Tracing the History of Ore Formation. In *Treatise in Geochemistry*, 2nd ed.; Turekian, K.K., Holland, H.D., Scott, S.D., Eds.; Pergamon Press: Oxford, UK, 2014; pp. 88–118.
40. Li, W.S.; Ni, P.; Pan, J.Y.; Fan, M.S.; Chen, L.L.; Zhang, D.; Wu, X.W.; Gao, Y. Constraints on the timing and genetic link of scheelite- and wolframite-bearing quartz veins in the chuankou W ore field, South China. *Ore Geol. Rev.* **2021**, *133*, 104122. [[CrossRef](#)]
41. Xiang, A.P.; Chen, Y.C.; She, H.Q.; Li, G.M.; Li, Y.X. Geochronology and geochemical characteristic of biotite granite of the Dayana W-Mo deposit in Dong Ujimqin Banner, Inner Mongolia, and its geological significance. *Acta Geol. Sin.* **2018**, *92*, 107–124.
42. Deng, X.D.; Luo, T.; Li, J.W.; Hu, Z.C. Direct dating of hydrothermal tungsten mineralization using in situ wolframite U-Pb chronology by laser ablation ICP-MS. *Chem. Geol.* **2019**, *515*, 94–104. [[CrossRef](#)]
43. Tang, Y.W.; Cui, K.; Zheng, Z.; Gao, J.F.; Han, J.J.; Yang, J.H.; Liu, L. LA-ICP-MS U Pb geochronology of wolframite by combining NIST series and common lead-bearing MTM as the primary reference material: Implications for metallogenesis of South China. *Gondwana Res.* **2020**, *83*, 217–231. [[CrossRef](#)]
44. Yang, M.; Yang, Y.H.; Wu, S.T.; Romer, R.L.; Che, X.D.; Zhao, Z.F.; Li, W.S.; Yang, J.H.; Wu, F.Y.; Xie, L.W.; et al. Accurate and precise in situ U-Pb isotope dating of wolframite series minerals via LA-SF-ICP-MS. *J. Anal. At. Spectrom.* **2020**, *35*, 2191–2203. [[CrossRef](#)]
45. Carr, P.A.; Mercadier, J.; Harlaux, M.; Romer, R.L.; Moreira, E.; Legros, H.; Cuney, M.; Marignac, C.; Cauzid, J.; Salsi, L.; et al. U/Pb geochronology of wolframite by LA-ICP-MS; mineralogical constraints, analytical procedures, data interpretation, and comparison with ID-TIMS. *Chem. Geol.* **2021**, *584*, 120511. [[CrossRef](#)]
46. Yang, S.W.; Lou, F.S.; Xu, C.; Feng, C.Y.; Cao, S.H.; Xu, D.R.; Tang, Y.W. Two significant quartz-wolframite-veining mineralization events in the Jiangnan Orogen, South China: Constraints from in-situ U-Pb dating of wolframite in the Dongping and Dahutang W-(Cu-Mo) deposits. *Ore Geol. Rev.* **2022**, *141*, 104598. [[CrossRef](#)]
47. Chen, P.W.; Zeng, Q.D.; Guo, W.K.; Chen, J.Q. The source, enrichment and precipitation of ore-forming elements for porphyry Mo deposit: Evidences from melt inclusions, biotite and fluorite in Dasuji deposit, China. *Ore Geol. Rev.* **2021**, *135*, 104205. [[CrossRef](#)]
48. Chen, P.W.; Liu, B.; Long, Z.; Zhou, L.L.; Fu, Y.; Zeng, Q.D. Ore genesis of the Sadaigoumen porphyry Mo deposit, North China Craton: Constraints from pyrite trace element and lead isotope analyses. *Ore Geol. Rev.* **2022**, *142*, 104698. [[CrossRef](#)]
49. Sun, G.T.; Zeng, Q.D.; Zhou, L.L.; Philip Hollis, S.; Zhou, J.X.; Chen, K.Y. Mechanisms for invisible gold enrichment in the Liaodong Peninsula, NE China: In situ evidence from the Xiaotongjiapuzi deposit. *Gondwana Res.* **2022**, *103*, 276–296. [[CrossRef](#)]
50. Cook, N.J.; Ciobanu, C.L.; Mao, J. Textural control on gold distribution in As-free pyrite from the Dongping, Huangtuliang and Hougou gold deposits, North China Craton (Hebei Province, China). *Chem. Geol.* **2009**, *264*, 101–121. [[CrossRef](#)]
51. Large, R.R.; Danyushevsky, L.; Hollit, C.; Maslennikov, V.; Meffre, S.; Gilbert, S.; Bull, S.; Scott, R.; Emsbo, P.; Thomas, H. Gold and trace element zonation in pyrite using a laser imaging technique: Implications for the timing of gold in orogenic and Carlin-style sediment-hosted deposits. *Econ. Geol.* **2009**, *104*, 635–668. [[CrossRef](#)]
52. Maslennikov, V.V.; Maslennikova, S.P.; Large, R.R.; Danyushevsky, L.V. Study of trace element zonation in vent chimneys from the Silurian Yaman-Kasay volcanic-hosted massive sulfide deposit (southern Urals, Russia) using laser ablation-inductively coupled plasma mass spectrometry (LA-ICPMS). *Econ. Geol.* **2009**, *104*, 1111–1141. [[CrossRef](#)]
53. Sung, Y.H.; Brugger, J.; Ciobanu, C.L.; Pring, A.; Skinner, W.; Nugus, M. Invisible gold in arsenian pyrite and arsenopyrite from amultistage Archaean gold deposit: Sunrise Dam, eastern goldfields province, Western Australia. *Miner. Depos.* **2009**, *44*, 765–791. [[CrossRef](#)]
54. Thomas, H.V.; Large, R.R.; Bull, S.W.; Maslennikov, V.; Berry, R.F.; Fraser, R.; Froud, S.; Moye, R. Pyrite and pyrrhotite textures and composition in sediments, laminated quartz veins, and reefs at Bendigo gold mine, Australia: Insights for ore genesis. *Econ. Geol.* **2011**, *106*, 1–31. [[CrossRef](#)]

55. Goldmann, S.; Melcher, F.; Gabler, H.E.; Dewaele, S.; Clercq, F.D.; Muchez, P. Mineralogy and trace element chemistry of ferberite/reinite from tungsten deposits in Central Rwanda. *Minerals* **2013**, *3*, 121–144. [[CrossRef](#)]
56. Xiong, Y.Q.; Shao, Y.J.; Zhou, H.D.; Wu, Q.H.; Liu, J.P.; Wei, H.T.; Zhao, R.C.; Cao, J.Y. Ore-forming mechanism of quartz-vein-type W-Sn deposits of the Xitian district in SE China: Implications from the trace element analysis of wolframite and investigation of fluid inclusions. *Ore Geol. Rev.* **2017**, *83*, 152–173. [[CrossRef](#)]
57. Zhang, Q.; Zhang, R.Q.; Gao, J.F.; Lu, J.J.; Wu, J.W. In-situ LA-ICP-MS trace element analyses of scheelite and wolframite: Constraints on the genesis of veinlet-disseminated and vein-type tungsten deposits, South China. *Ore Geol. Rev.* **2018**, *99*, 166–179. [[CrossRef](#)]
58. Xiong, Y.Q.; Shao, Y.J.; Cheng, Y.B.; Jiang, S.Y. Discrete Jurassic and Cretaceous Mineralization Events at the Xiangdong W(-Sn) Deposit, Nanling Range, South China. *Econ. Geol.* **2020**, *115*, 385–413. [[CrossRef](#)]
59. Xiong, Z.R.; Li, X.N.; Qi, C.; Xiong, Y.Q. Geochronology of cassiterite and trace element compositions of wolframite: Constraints to the ore genesis of Jiguanshi tungsten deposit, eastern Hunan Province. *Acta Petrol. Sin.* **2021**, *37*, 769–780.
60. Wang, J. Chronology and Geochemistry of Granitoid for the Weilasituo Copper polymetal Deposit in Inner Mongolia. Master's Thesis, China University of Geosciences, Beijing, China, 2009.
61. Dai, X.L. The Characteristics of Granite Mass and Mineralization in the Outer Liner of Baishitouwa Tungsten Mineral Deposit, Taipusiqi City, Inner Mongolia. Master's Thesis, Central South University, Changsha, China, 2008.
62. IMBGMR (Inner Mongolian Bureau of Geology Mineral Resources). *Regional Geology of Inner Mongolia*; Geological Publishing House: Beijing, China, 1991; pp. 1–725.
63. Sengör, A.M.C.; Natal'in, B.A.; Burtman, V.S. Evolution of the Altaid tectonic collage and Paleozoic crustal growth in Eurasia. *Nature* **1993**, *364*, 299–307. [[CrossRef](#)]
64. Xiao, W.J.; Santosh, M. The western Central Asian Orogenic Belt: A window to accretionary orogenesis and continental growth. *Gondwana Res.* **2014**, *25*, 1429–1444. [[CrossRef](#)]
65. Eizenhöfer, P.R.; Zhao, G.C.; Zhang, J.; Sun, M. Final closure of the Paleo-Asian Ocean along the Solonker suture zone: Constraints from geochronological and geochemical data of Permian volcanic and sedimentary rocks. *Tectonics* **2014**, *33*, 441–463. [[CrossRef](#)]
66. Li, Y.; Xu, W.L.; Tang, J.; Sun, C.Y.; Zhang, X.M.; Xiong, S. Late Paleozoic igneous rocks in the Xing'an Massif and its amalgamation with the Songnen Massif, NE China. *J. Asian Earth Sci.* **2020**, *197*, 104407. [[CrossRef](#)]
67. Zhao, L.; Li, Z.; Li, J.Y.; Guo, F. Generation of Triassic post-collisional granitoids in the Linxi region (Inner Mongolia, NE China) and crustal growth in the eastern Central Asian Orogenic Belt through melting of relict oceanic crust. *J. Asian Earth Sci.* **2019**, *171*, 348–362. [[CrossRef](#)]
68. Zhang, X.N.; Zeng, Q.D.; Nie, F.J. Geochemical variations of the Late Paleozoic granitoids from the Baolidao arc-accretion belt in southeastern segment of Central Asia Orogenic Belt: Implications for tectonic transition from Early Carboniferous to Early Permian. *J. Earth Sci.* **2022**, 1–17. [[CrossRef](#)]
69. Li, H.H.; Yu, J.J.; Guo, X.W.; Xu, W.L. Late Permian medium-pressure metamorphism in the eastern Songnen Massif, eastern Central Asian Orogenic Belt (NE China): Implications for the final closure of the Paleo-Asian Ocean. *J. Asian Earth Sci.* **2021**, *215*, 104800. [[CrossRef](#)]
70. Shen, X.L.; Du, Q.X.; Han, Z.Z.; Song, Z.G.; Han, C.; Zhong, W.J.; Ren, X. Constraints of zircon U-Pb-Hf isotopes from Late Permian-Middle Triassic flora-bearing strata in the Yanbian area (NE China) on a scissor-like closure model of the Paleo-Asian Ocean. *J. Asian Earth Sci.* **2019**, *183*, 103964. [[CrossRef](#)]
71. Chen, P.W.; Zeng, Q.D.; Wang, Y.B.; Zhou, T.C.; Yu, B.; Chen, J.Q. Petrogenesis of the Dasuji porphyry Mo deposit at the northern margin of North China Craton: Constrains from geochronology, geochemistry and isotopes characteristics. *Lithos* **2018**, *322*, 87–103. [[CrossRef](#)]
72. Chen, P.W.; Zeng, Q.D.; Zhou, T.C. Petrogenesis and Mo prospecting significance of Sadaigoumen granites on the northern margin of the North China Craton. *J. Geochem. Explor.* **2020**, *214*, 106536. [[CrossRef](#)]
73. Zorin, Y.A. Geodynamics of the western part of the Mongol-Okhotsk collisional belt, Trans-Baikal region (Russia) and Mongolia. *Tectonophysics* **1999**, *306*, 33–56. [[CrossRef](#)]
74. Ma, X.H.; Zhu, W.P.; Zhou, Z.H.; Qiao, S.L. Transformation from Paleo-Asian Ocean closure to Paleo-Pacific subduction: New constraints from granitoids in the eastern Jilin-Heilongjiang Belt, NE China. *J. Asian Earth Sci.* **2017**, *144*, 261–286. [[CrossRef](#)]
75. Pang, Y.M.; Guo, X.W.; Zhang, X.H.; Zhu, X.Q.; Hou, F.H.; Wen, Z.H.; Han, Z.Z. Late Mesozoic and Cenozoic tectono-thermal history and geodynamic implications of the Great Xing'an Range, NE China. *J. Asian Earth Sci.* **2020**, *189*, 104155. [[CrossRef](#)]
76. Zhang, P.H.; Fang, H.; Zhong, Q.; Zhang, X.B.; Yuan, Y.Z.; Liu, J.X. Structural features and tectonic evolution of the Nenjiang–Balihan fault in the western margin of the Songliao Basin, NE China, inferred from 2D inversion of magnetotelluric data. *J. Asian Earth Sci.* **2021**, *206*, 104628. [[CrossRef](#)]
77. Chen, L.; Liang, C.Y.; Neubauer, F.; Liu, Y.J.; Zhang, Q.; Song, Z.W. Sedimentary processes and deformation styles of the Mesozoic sedimentary succession in the northern margin of the Mohe basin, NE China: Constraints on the final closure of the Mongol–Okhotsk Ocean. *J. Asian Earth Sci.* **2021**, 105052. [[CrossRef](#)]
78. Zhang, G.L.; Xie, W.; Wen, S.Q.; Gong, E.P.; Guo, R.R.; Tang, T.Q. Petrogenesis and tectonic implications of Late Mesozoic volcanic rocks in the northern and central Great Xing'an Range, NE China: Constraints from geochronology and geochemistry. *Geol. J.* **2020**, *55*, 8282–8308. [[CrossRef](#)]

79. Zeng, Q.D.; Liu, J.M.; Yu, C.M.; Ye, J.; Liu, H.T. Metal deposits in the Da Hinggan Mountains, NE China: Styles, characteristics, and exploration potential. *Int. Geol. Rev.* **2011**, *53*, 846–878. [\[CrossRef\]](#)
80. Wu, Z.J.; Yang, X.Y.; Ma, Y.S.; Sun, S.J.; Han, X.Z.; Zheng, Y.Z.; Li, S. A synthesis of geochemistry of Mesozoic igneous rocks in NE China and tectonic superposition and transformation of the easternmost Central Asian Orogenic Belt. *J. Asian Earth Sci.* **2021**, *227*, 105032. [\[CrossRef\]](#)
81. IMLGE (Inner Mongolian Longwang Geological Exploration Co., Ltd.). *Prospecting Report of Baishitouwa W Deposit in Taipusi Banner, Inner Mongolia Autonomous Region*; IMLGE: Chifeng, China, 2011; pp. 1–80.
82. Lecumberri-Sanchez, P.; Romer, R.L.; Lüders, V.; Bodnar, R.J. Genetic relationship between silver-lead-zinc mineralization in the Wutong deposit, Guangxi Province and Mesozoic granitic magmatism in the Nanling belt, southeast China. *Miner. Depos.* **2014**, *49*, 353–369. [\[CrossRef\]](#)
83. Tang, Y.W.; Gao, J.F.; Lan, T.G.; Cui, K.; Han, J.J.; Zhang, X.; Chen, Y.W.; Chen, Y.H. In situ low-U garnet U-Pb dating by LA-SF-ICP-MS and its application in constraining the origin of Anji skarn system combined with Ar-Ar dating and Pb isotopes. *Ore Geol. Rev.* **2021**, *130*, 103970. [\[CrossRef\]](#)
84. Liu, Y.S.; Hu, Z.C.; Zong, K.Q.; Gao, C.G.; Gao, S.; Xu, J.; Chen, H.H. Reappraisal and refinement of zircon U-Pb isotope and trace element analyses by LA-ICP-MS. *Chin. Sci. Bull.* **2010**, *55*, 1535–1546. [\[CrossRef\]](#)
85. Chew, D.M.; Sylvester, P.J.; Tubrett, M.N. U-Pb and Th-Pb dating of apatite by LA-ICPMS. *Chem. Geol.* **2011**, *280*, 200–216. [\[CrossRef\]](#)
86. Roberts, N.M.; Rasbury, E.T.; Parrish, R.R.; Smith, C.J.; Horstwood, M.S.; Condon, D.J. A calcite reference material for LA-ICP-MS U-Pb geochronology. *Geochem. Geophys. Geosy.* **2017**, *18*, 2807–2814. [\[CrossRef\]](#)
87. Luo, T.; Deng, X.D.; Li, J.W.; Hu, Z.C.; Zhang, W.; Liu, Y.S.; Zhang, J.F. U-Pb geochronology of wolframite by laser ablation inductively coupled plasma mass spectrometry. *J. Anal. At. Spectrom.* **2019**, *34*, 1439–1446. [\[CrossRef\]](#)
88. Liu, Y.S.; Hu, Z.C.; Gao, S.; Günther, D.; Xu, J.; Gao, C.G.; Chen, H.H. In situ analysis of major and trace elements of anhydrous minerals by LA-ICP-MS without applying an internal standard. *Chem. Geol.* **2008**, *257*, 34–43. [\[CrossRef\]](#)
89. Hu, Z.C.; Liu, Y.S.; Gao, S.; Xiao, S.Q.; Zhao, L.S.; Günther, D.; Li, M.; Zhang, W.; Zong, K.Q. A “wire” signal smoothing device for laser ablation inductively coupled plasma mass spectrometry analysis. *Spectrochim. Acta Part B At. Spectrosc.* **2012**, *78*, 50–57. [\[CrossRef\]](#)
90. Zhang, W.; Lentz, D.R.; Thorne, K.G.; Massawe, R.J.R. Late Silurian-Early Devonian slab break-off beneath the Canadian Appalachians: Insights from the Nashwaak Granite, west-central New Brunswick, Canada. *Lithos* **2020**, *358*, 105393. [\[CrossRef\]](#)
91. Rudnick, R.L.; Gao, S. 3.01—Composition of the continental crust. *Treatise Geochem.* **2003**, *3*, 659.
92. Shannon, R.D. Revised effective ionic radii and systematic studies of interatomic distances in halides and chalcogenides. *Acta Crystallogr.* **1976**, *32*, 751–767. [\[CrossRef\]](#)
93. Polya, D.A. Compositional variation in wolframites from the Barroca Grande mine, Portugal: Evidence for fault-controlled ore formation. *Mineral. Mag.* **1988**, *52*, 497–503. [\[CrossRef\]](#)
94. Tindle, A.G.; Webb, P.C. Niobian wolframite from Glen Gairn in the Eastern Highlands of Scotland: A microprobe investigation. *Geochim. Cosmochim. Acta* **1989**, *53*, 1921–1935. [\[CrossRef\]](#)
95. Černý, P.; Ercit, T.S. Mineralogy of niobium and tantalum: Crystal chemical relationships, paragenetic aspects and their economic implications. In *Lanthanides, Tantalum and Niobium*; Möller, P., Černý, P., Saupé, F., Eds.; Springer: Berlin/Heidelberg, Germany, 1989; pp. 27–79.
96. Černý, P.; Novák, M.; Chapman, R.; Ferreira, K.J. Subsolidus behavior of niobian rutile from the Písek region, Czech Republic: A model for exsolution in W- and Fe<sup>2+</sup> >> Fe<sup>3+</sup>-rich phases. *J. Geosci.* **2007**, *52*, 143–159. [\[CrossRef\]](#)
97. Tindle, A.G.; Breaks, F.W.; Webb, P.C. Wodginite-group minerals from the Separation Rapids rare-element granitic pegmatite group, northwestern Ontario. *Can. Mineral.* **1998**, *36*, 637–658.
98. Beddoestephens, B.; Fortey, N.J. Columbite from the Carrock Fell tungsten deposit. *Mineral. Mag.* **1981**, *44*, 217–223. [\[CrossRef\]](#)
99. Gan, G.L.; Chen, Z.X. Compositional characteristics of wolframite in tin deposits, Dupangling, Guangxi. *Chin. J. Geochem.* **1992**, *11*, 156–167. [\[CrossRef\]](#)
100. Raimbault, L.; Baumer, A.; Dubru, M.; Benkerrou, C.; Croze, V.; Zahm, A. REE fractionation between scheelite and apatite in hydrothermal conditions. *Am. Mineral.* **1993**, *78*, 1275–1285.
101. Ghaderi, M.; Palin, J.M.; Campbell, I.H.; Sylvester, P.J. Rare earth element systematics in scheelite from hydrothermal gold deposits in the Kalgoorlie-Norseman region, Western Australia. *Econ. Geol.* **1999**, *94*, 423–437. [\[CrossRef\]](#)
102. Mateus, A.; Figueiras, J.; Martins, I.; Rodrigues, P.; Pinto, F. Relative Abundance and Compositional Variation of Silicates, Oxides and Phosphates in the W-Sn-Rich Lodes of the Panasqueira Mine (Portugal): Implications for the Ore-Forming Process. *Minerals* **2020**, *10*, 551. [\[CrossRef\]](#)
103. Bau, M. Controls on the fractionation of isovalent trace elements in magmatic and aqueous systems: Evidence from Y/Ho, Zr/Hf, and lanthanide tetrad effect. *Contrib. Mineral. Petr.* **1996**, *123*, 323–333. [\[CrossRef\]](#)
104. Kempe, U.; Wolf, D. Anomalously high Sc contents in ore minerals from Sn-W deposits: Possible economic significance and genetic implications. *Ore Geol. Rev.* **2006**, *28*, 103–122. [\[CrossRef\]](#)
105. Zhang, D.H. *Geochemistry of Ore-Forming Process*; Geological Publishing House: Beijing, China, 2015.
106. Liu, Y.J.; Cao, L.M. *Introduction to Elemental Geochemistry*; Geological Publishing House: Beijing, China, 1987; pp. 1–112.
107. Zhang, C.Z. Variation in Nb-Ta contents of wolframite and its significance as an indicator. *Miner. Depos.* **1984**, *2*, 59–67.

108. Ballouard, C.; Poujol, M.; Boulvais, P.; Branquet, Y.; Tartèse, R.; Vignerresse, J.L. Nb-Ta fractionation in peraluminous granites: A marker of the magmatic-hydrothermal transition. *Geology* **2016**, *44*, 231–234. [[CrossRef](#)]
109. Zhang, Y.X. Some geochemical data on scandium. *Sci. Geol. Sin.* **1959**, *11*, 345–349.
110. Yuan, L.L.; Chi, G.X.; Wang, M.Q.; Li, Z.H.; Xu, D.R.; Deng, T.; Geng, J.Z.; Hu, M.Y.; Zhang, L. Characteristics of REEs and trace elements in scheelite from the Zhuxi W deposit, South China: Implications for the ore-forming conditions and processes. *Ore Geol. Rev.* **2019**, *109*, 585–597. [[CrossRef](#)]
111. Bau, M.; Dulski, P. Comparative study of yttrium and rare-earth element behaviours in fluorine-rich hydrothermal fluids. *Contrib. Mineral. Petr.* **1995**, *119*, 213–223. [[CrossRef](#)]
112. Cao, J.Y.; Li, H.; Algeo, T.J.; Yang, L.Z.; Tamehe, L.S. Two-stage magmatism and tungsten mineralization in the Nanling Range, South China: Evidence from the Jurassic Helukou deposit. *Am. Mineral.* **2021**, *106*, 1488–1502. [[CrossRef](#)]
113. Zhang, D.X.; Pan, J.Q.; Gao, J.F.; Dai, T.G.; Bayless, R.C. In situ LA ICP-MS analysis of trace elements in scheelite from the Xuefeng Uplift Belt, South China and its metallogenic implications. *Ore Geol. Rev.* **2021**, *133*, 104097. [[CrossRef](#)]
114. Singh, S.K.; Singh, S. Geochemistry and tungsten metallogeny of the Balda granite, Rajasthan. India. *Gondwana Res.* **2001**, *4*, 487–495. [[CrossRef](#)]
115. Fogliata, A.S.; Baez, M.A.; Hagemann, S.G.; Santos, J.O.; Sardi, F. Post-orogenic, Carboniferous granite-hosted Sn-W mineralization in the Sierras Pampeanas Orogen, Northwestern Argentina. *Ore Geol. Rev.* **2012**, *45*, 16–32. [[CrossRef](#)]
116. Mao, J.W.; Cheng, Y.B.; Chen, M.H.; Franco, P. Major types and time–space distribution of Mesozoic ore deposits in South China and their geodynamic settings. *Miner. Depos.* **2013**, *48*, 267–294.
117. Huang, L.C.; Jiang, S.Y. Highly fractionated S-type granites from the giant Dahutang tungsten deposit in Jiangnan orogen, southeast China: Geochronology, petrogenesis and their relationship with W-mineralization. *Lithos* **2014**, *202*, 207–226. [[CrossRef](#)]
118. Zhang, Y.; Yang, J.H.; Chen, J.Y.; Wang, H.; Xiang, Y.X. Petrogenesis of Jurassic tungsten-bearing granites in the Nanling Range, South China: Evidence from whole-rock geochemistry and zircon U–Pb and Hf–O isotopes. *Lithos* **2017**, *278*, 166–180. [[CrossRef](#)]
119. Jiang, H.; Jiang, S.Y.; Li, W.Q.; Zhao, K.D.; Peng, N.J. Highly fractionated Jurassic I-type granites and related tungsten mineralization in the Shirenzhang deposit, northern Guangdong, south China: Evidence from cassiterite and zircon U–Pb ages, geochemistry and Sr–Nd–Pb–Hf isotopes. *Lithos* **2018**, *312*, 186–203. [[CrossRef](#)]
120. Yuan, S.D.; Williams-Jones, A.E.; Mao, J.W.; Zhao, P.L.; Yan, C.; Zhang, D.L. The origin of the Zhangjialong tungsten deposit, South China: Implications for W–Sn mineralization in large granite batholiths. *Econ. Geol.* **2018**, *113*, 1193–1208. [[CrossRef](#)]
121. Steiner, B.M. W and Li–Cs–Ta geochemical signatures in I-type granites—A case study from the Vosges Mountains, NE France. *J. Geochem. Explor.* **2019**, *197*, 238–250. [[CrossRef](#)]
122. Cao, J.Y.; Wu, Q.H.; Yang, X.Y.; Deng, X.T.; Li, H.; Kong, H.; Xi, X.S. Geochemical factors revealing the differences between the Xitian and Dengfuxian composite plutons, middle Qin–Hang Belt: Implications to the W–Sn mineralization. *Ore Geol. Rev.* **2020**, *118*, 103353. [[CrossRef](#)]
123. Li, J.; Huang, X.L.; Fu, Q.; Li, W.X. Tungsten mineralization during the evolution of a magmatic-hydrothermal system: Mineralogical evidence from the Xihuashan rare-metal granite in South China. *Am. Mineral.* **2021**, *106*, 443–460. [[CrossRef](#)]
124. Feng, Y.Y.; Fu, W.; Feng, Z.H.; Yang, J.W.; Li, Z.Y.; Le, X.W.; Li, S.S.; Feng, M.; Wang, C.Z.; Xu, J.F. Petrogenesis and metallogenesis of an extraordinary deeply hidden granite pluton overlain by W–Zn–Pb–Ag-mineralized roof: Example from Xidamingshan district, South China. *Ore Geol. Rev.* **2021**, *130*, 103932. [[CrossRef](#)]
125. Sun, K.K.; Chen, B. Trace elements and Sr–Nd isotopes of scheelite: Implications for the W–Cu–Mo polymetallic mineralization of the Shimensi deposit, South China. *Am. Mineral.* **2017**, *102*, 1114–1128.
126. Yang, C.; Zhao, H.J.; Zhao, P.L.; Yuan, S.D. Muscovite Ar–Ar isotopic dating of Zhenkou quartz vein type wolframite deposit in southern Hunan Province and its significance for regional exploration. *Miner. Depos.* **2019**, *38*, 1147–1158.
127. Brugger, J.; Lahaye, Y.; Costa, S.; Lambert, D.; Bateman, R. Inhomogeneous distribution of REE in scheelite and dynamics of Archaean hydrothermal systems (Mt. Charlotte and Drysdale gold deposits, Western Australia). *Contrib. Mineral. Petr.* **2000**, *139*, 251–264. [[CrossRef](#)]
128. Zhu, Y.N.; Peng, J.T.; Liu, S.Y.; Sun, Y.Z. Mineral deposit geology and trace element geochemistry of wolframite from the Woxi deposit, western Hunan, China. *Geochimica* **2014**, *43*, 287–300.